Efficient broadband vibration energy harvesting using multiple piezoelectric bimorphs

Hamed Farokhi [a], Alireza Gholipour [b], Mergen H. Ghayesh [b,*]

[a] *Department of Mechanical and Construction Engineering, Northumbria University, Newcastle upon Tyne, NE1 8ST, UK*
[b] *School of Mechanical Engineering, University of Adelaide, South Australia 5005, Australia*
**Corresponding author: mergen.ghayesh@adelaide.edu.au*
Email: (H Farokhi): hamed.farokhi@northumbria.ac.uk
Email: (A Gholipour): alireza.gholipour@adelaide.edu.au

Abstract

This paper presents complete nonlinear electromechanical models for energy harvesting devices consisting of multiple piezoelectric bimorphs connected in parallel and series, for the first time. The proposed model is verified against available experimental results for a specific case. The piezoelectric and beam constitutive equations and different circuit equations are utilised to derive the complete nonlinear models for series and parallel connections of the piezoelectric bimorphs (PBs) as well as those of piezoelectric layers in each bimorph, i.e. four nonlinear models in total. A multi-modal Galerkin approach is used to discretise these nonlinear electromechanical models. The resultant high-dimensional set of equations is solved utilising a highly optimised and efficient numerical continuation code. Examining the system behaviour shows that the optimum load resistance for an energy harvester array of 4 PBs connected in parallel is almost 4% of that for the case with PBs connected in series. It is shown an energy harvesting array of 8 PBs could reach a bandwidth of 14 Hz in low frequency range, i.e. 20-34 Hz. Compared to an energy harvester with 1 PB, it is shown that the bandwidth can be increased by more than 300% using 4 PBs and by more than 500% using 8 PBs. Additionally, the drawbacks of a multi-PB energy harvesting device are identified and design enhancements are proposed to improve the efficiency of the device.

Keywords: Piezoelectric bimorph; Nonlinear model; Broadband energy harvesting; multi-frequency resonance.

1. Introduction

Environmental vibration is a source of energy which can be used to power small wireless electronics and sensors, such as MEMS devices [1-11], to make them power-autonomous and to remove the need for a battery for their continuous operation [12-14]. A vibration-based energy harvester is a device which captures the ambient vibration (originating, for instance, from fluid flow or machinery operation) and converts it into electric energy. The main limitation of vibration energy harvesters is that they often operate effectively within a narrow environmental vibration frequency band. Hence, their efficiency could drop significantly if the input vibration is not within that specific operating range. This limitation has motivated many researchers to come up with methods for widening the operating bandwidth of vibration energy harvesters. In what follows, a review of some of the studies in the literature is given.

As one of the earlier studies on this topic, Dutoit et al. [15] proposed various piezoelectric-based energy harvester designs for micro-scale sensors. Different kinds of piezoelectric energy harvesters were studied by Sodano et al. [16], who performed experimental analysis to examine their capabilities for recharging a battery. The investigations were continued by Soliman et al. [17], who proposed an electromagnetic harvester while implementing a piecewise-linear oscillator element; they performed experimental and theoretical investigations, with the latter being based on a single-mode

model. A design for an electromagnetic micro energy harvester for low vibration frequencies was developed by Beeby et al. [18] through use of discrete components. Xue et al. [19] developed an analytical solution to the response of a multi-bimorph energy harvesting device connected in parallel and series through use of a single-mode linear model of the piezoelectric bimorph. Experimental investigations were performed by Mann and Sims [20] on a magnetic energy harvesting device; they conducted theoretical analysis as well utilising a single-mode duffing-type model. Another theoretical-experimental investigation on vibration energy harvesters was conducted by Erturk and Inman [21]; they proposed an analytical solution for a single-mode linear made a comparison between theoretical results and experimental observations. Influences of an added tip mass on the performance of an energy harvester was examined by Kim et al. [22], who employed a single-mode linear model for theoretical calculations.

These investigations were continued by Lumentut et al. [23] who examined the multi-frequency energy harvesting of a multi-electromechanical piezoelectric bimorph system analytically based on a single-mode model in a linear regime. Nguyen and Halvorsen [24] analysed the effect of softening-type springs on the output of a micro version of the system. A single-mode truncated model was utilised by Firoozy et al. [25] for a piezoelectric unimorph system with a magnet as the proof mass under harmonic base motion. A vibration-based energy harvester configuration with a magnetoelectric composite and a permanent magnet proof mass was proposed by Ju et al. [26]. Zhao and Yang [27] introduced a mechanical constraint to an energy harvester operating on wind flow and base vibration.

This investigation presents, as the first endeavour, complete nonlinear models for multi-modal electro/mechanical analysis of energy harvester devices consisting of multiple piezoelectric bimorphs (PBs) connected in parallel or series. More specifically, the equations of motion of a multi-PB energy harvester are obtained while taking into account the geometric and inertial nonlinearities arising from large rotation of the cantilever. Additionally, the nonlinear circuit equations are obtained for various cases, i.e. parallel and series connections of piezoelectric layers in a PB as well as parallel and series connection of PBs in an energy harvester. The developed model is verified for a specific case from the literature. The multi-frequency electromechanical behaviours of different cases are examined in detail through construction of frequency response diagrams. The numerical results show that the proof mass can be effectively used to tune the resonance frequencies of a multi-PB energy harvesting device. It is shown that the difference between the natural frequencies of the PBs is a significantly important parameter in determining the energy harvester's operating resonance bandwidth as well as its power output level in the operating region. Furthermore, through conducting a detailed parametric analysis on the proposed nonlinear model, design enhancements are proposed to improve the efficiency of multi-PB energy harvesting devices.

2. Complete nonlinear electromechanical models for multi-PB energy harvesters

In this section, complete nonlinearly coupled electromechanical models of energy harvester devices consisting of an array of cantilever piezoelectric bimorphs connected in parallel or series are developed using Euler-Bernoulli beam model, one-dimensional piezoelectric equations, and electrical circuit equations. In particular, an array of cantilever

PBs is considered as shown in Fig. 1, with the whole system being under base motion of $z_b\sin(\omega_b t)$, with z_b and ω_b denoting respectively the amplitude and frequency of the base motion. Four different configurations can be considered for an array of cantilever PBs depending on the connection type of the piezoelectric layers in the bimorph as well as the connection type of the PBs in the array, as shown in Fig. 2. The complete nonlinear electromechanical models for each of these four cases will be derived in detail in this section. It is assumed that in each bimorph the piezoelectric layers cover the substrate from $l_1^{(j)}$ to $l_2^{(j)}$; this results in the piezoelectric layers length of $l_2^{(j)} - l_1^{(j)}$ which is denoted by $L_p^{(j)}$ in this section; *j* denotes the number of the PB. The material properties of the bimorphs are assumed to be the same. In each bimorph, all layers have the same width, $b^{(j)}$; $t_s^{(j)}$ denotes the thickness of the substrate while $t_p^{(j)}$ denotes the thickness of each piezoelectric layer. $M_p^{(j)}$ represents the proof mass in the *j*th PB. The length of substrate in all PBs is the same and equal to *L*.

2.1 Nonlinear electromechanical model of the jth cantilever piezoelectric bimorph

In this section, the nonlinear equations of motion of the *j*th cantilever piezoelectric bimorph are derived. The detailed derivation procedure is given and the final equations of motion are reported for both parallel/series connection-types of piezoelectric layers in a bimorph. These equations are then used in the following sections to construct the complete nonlinear model for an array of cantilever piezoelectric bimorphs connected in parallel or series.

Considering inextensibility condition, the axial stress/strain developed in the *j*th-cantilever bimorph can be respectively formulated as

$$\sigma_s^{(j)} = E_s \varepsilon_1^{(j)}, \tag{1}$$

$$\varepsilon_1^{(j)} = -z\left(\frac{\partial^2 w^{(j)}}{\partial x^2} + \frac{1}{2}\frac{\partial^2 w^{(j)}}{\partial x^2}\left(\frac{\partial w^{(j)}}{\partial x} \right)^2 \right), \tag{2}$$

in which E_s represents Young's modulus; $w^{(j)}$ stands for the transverse displacement in the *j*th PB and *z* denotes the distance from the midplane of the substrate layer. Constitutive equations of the top and bottom piezoelectric layers of the *j*th cantilever bimorph is respectively given by

$$\begin{aligned} \sigma_{pz(top)}^{(j)} &= c_{11}\varepsilon_1^{(j)} - h_{31}D_{3(top)}^{(j)}, \\ E_{3(top)}^{(j)} &= -h_{31}\varepsilon_1^{(j)} + \beta_{33}D_{3(top)}^{(j)}, \\ \sigma_{pz(bot)}^{(j)} &= c_{11}\varepsilon_1^{(j)} - h_{31}D_{3(bot)}^{(j)}, \\ E_{3(bot)}^{(j)} &= -h_{31}\varepsilon_1^{(j)} + \beta_{33}D_{3(bot)}^{(j)}, \end{aligned} \tag{3}$$

in which D_3 and E_3 denote the electric-displacement/electric-field in *z* direction; the *j*th superscript indicates the number of the PB while the "top" and "bot" subscripts indicate the top and bottom piezoelectric layers in the *j*th PB. c_{11} , h_{31}, β_{31} are piezoelectric constants which can be expressed as

$$c_{11} = \left(s_{11} - d_{31}^2/\xi_{33} \right)^{-1}, \; h_{31} = -\left(d_{31} - s_{11}\xi_{33}/d_{31} \right)^{-1}, \qquad \beta_{33} = \left(\xi_{33} - d_{31}^2/s_{11} \right)^{-1}, \tag{4}$$

in which s_{11}, d_{31}, and ξ_{33} denote the short-circuit compliance coefficient, the strain constant, and the dielectric constant, respectively.

The kinetic energy associated with the motion of the *j*th PB under base excitation is given by

$$KE^{(j)} = \int_0^L m^{(j)}(x)\left[\left(\int_0^x \frac{\partial w^{(j)}}{\partial x}\frac{\partial^2 w^{(j)}}{\partial t \partial x}\mathrm{d}x\right)^2 + \left(z_b\omega_b\cos(\omega_b t) + \frac{\partial w^{(j)}}{\partial t}\right)^2\right]\mathrm{d}x,$$
$$m^{(j)}(x) = \rho_s A_s^{(j)} + M_p^{(j)}\delta_D(x-L) + 2G^{(j)}(x)\rho_p A_p^{(j)}, \quad (5)$$
$$G^{(j)}(x) = H_v\left(x - l_1^{(j)}\right) - H_v\left(x - l_2^{(j)}\right),$$

in which ρ_p and $A_p^{(j)}$ are the mass density and cross-sectional area of the piezoelectric layers, ρ_s and $A_s^{(j)}$ are those of the substrate, and $M_p^{(j)}$ is the proof mass. H_v represents the Heaviside function while δ_D stands for the Dirac delta function.

For both parallel/series piezoelectric layers connections, the virtual work done by the voltages induced on the top and bottom piezoelectric layers are formulated as [28]

$$\delta W_e^{(j)} = \int_0^L b^{(j)} G^{(j)}(x)\left[V_{bot}^{(j)}(t)\delta D_{3(bot)}^{(j)} - V_{top}^{(j)}(t)\delta D_{3(top)}^{(j)}\right]\mathrm{d}x. \quad (6)$$

The work of the linear viscous damping is given by

$$\delta W_D^{(j)} = -\int_0^L c_d(x)\left[\left(z_b\omega_b\cos(\omega_b t) + \frac{\partial w^{(j)}}{\partial t}\right)\delta w^{(j)}\right]\mathrm{d}x,$$
$$c_d^{(j)}(x) = c_d\left(1 + 2G^{(j)}(x)\frac{A_p^{(j)}}{A_s^{(j)}}\right), \quad (7)$$

in which c_d is the damping coefficient.

The variations of the strain energy of the substrate is expressed as [21]

$$\delta\Pi_s^{(j)} = \int_0^L \int_{A_s^{(j)}} E_s\varepsilon_1\delta\varepsilon_1\,\mathrm{d}A\mathrm{d}x = \int_0^L \left\{E_s I_s^{(j)}\left[\left(\frac{1}{2}\left(\frac{\partial w^{(j)}}{\partial x}\right)^2 + 1\right)\frac{\partial^2 w^{(j)}}{\partial x^2}\right]\delta\left[\left(\frac{1}{2}\left(\frac{\partial w^{(j)}}{\partial x}\right)^2 + 1\right)\frac{\partial^2 w^{(j)}}{\partial x^2}\right]\right\}\mathrm{d}x, \quad (8)$$

in which $A_s^{(j)}$ and $I_s^{(j)}$ are the *j*th substrate cross area and its second moment, respectively.

For the top and bottom piezoelectric layers, the variation of the strain energy is given respectively by [28]

$$\begin{aligned}\delta\Pi_{pz(top)}^{(j)} &= \int_{l_1^{(j)}}^{l_2^{(j)}}\int_{A_p^{(j)}}\left[\left(c_{11}\varepsilon_1^{(j)}-h_{31}D_{3(top)}^{(j)}\right)\delta\varepsilon_1+\left(-h_{31}\varepsilon_1^{(j)}+\beta_{33}D_{3(top)}^{(j)}\right)\delta D_{3(top)}^{(j)}\right]\mathrm{d}A\mathrm{d}x \\ &= \int_{l_1^{(j)}}^{l_2^{(j)}}\left\{\left(\frac{1}{3}c_{11}b^{(j)}\left[\left(t_p^{(j)}\right)^3+3\left(t_p^{(j)}\right)^2\left(\frac{t_s^{(j)}}{2}\right)+3t_p^{(j)}\left(\frac{t_s^{(j)}}{2}\right)^2\right]\right)\left[\left(\frac{1}{2}\frac{\partial^2 w^{(j)}}{\partial x^2}\right)\left(\frac{\partial w^{(j)}}{\partial x}\right)^2+\frac{\partial^2 w^{(j)}}{\partial x^2}\right]\right. \\ &\qquad \left.\times\delta\left[\left(\frac{1}{2}\frac{\partial^2 w^{(j)}}{\partial x^2}\right)\left(\frac{\partial w^{(j)}}{\partial x}\right)^2+\frac{\partial^2 w^{(j)}}{\partial x^2}\right]\right\}\mathrm{d}x+\int_{l_1^{(j)}}^{l_2^{(j)}}\beta_{33}A_p^{(j)}D_{3(top)}^{(j)}\delta D_{3(top)}^{(j)}\,\mathrm{d}x \\ &\quad +\int_{l_1^{(j)}}^{l_2^{(j)}}\left(\frac{1}{2}\left(t_s^{(j)}+t_p^{(j)}\right)h_{31}A_p^{(j)}\right)\left\{\left[\left(\frac{1}{2}\frac{\partial^2 w^{(j)}}{\partial x^2}\right)\left(\frac{\partial w^{(j)}}{\partial x}\right)^2+\frac{\partial^2 w^{(j)}}{\partial x^2}\right]\delta D_{3(top)}^{(j)}\right. \\ &\qquad \left.+D_{3(top)}^{(j)}\delta\left[\left(\frac{1}{2}\frac{\partial^2 w^{(j)}}{\partial x^2}\right)\left(\frac{\partial w^{(j)}}{\partial x}\right)^2+\frac{\partial^2 w^{(j)}}{\partial x^2}\right]\right\}\mathrm{d}x,\end{aligned} \tag{9}$$

$$\begin{aligned}\delta\Pi_{pz(bot)}^{(j)} &= \int_{l_1^{(j)}}^{l_2^{(j)}}\int_{A_p^{(j)}}\left[\left(c_{11}\varepsilon_1^{(j)}-h_{31}D_{3(bot)}^{(j)}\right)\delta\varepsilon_1+\left(-h_{31}\varepsilon_1^{(j)}+\beta_{33}D_{3(bot)}^{(j)}\right)\delta D_{3(bot)}^{(j)}\right]\mathrm{d}A\mathrm{d}x \\ &= \int_{l_1^{(j)}}^{l_2^{(j)}}\left\{\left(\frac{1}{3}c_{11}b^{(j)}\left[\left(t_p^{(j)}\right)^3+3\left(t_p^{(j)}\right)^2\left(\frac{t_s^{(j)}}{2}\right)+3t_p^{(j)}\left(\frac{t_s^{(j)}}{2}\right)^2\right]\right)\left[\left(\frac{1}{2}\frac{\partial^2 w^{(j)}}{\partial x^2}\right)\left(\frac{\partial w^{(j)}}{\partial x}\right)^2+\frac{\partial^2 w^{(j)}}{\partial x^2}\right]\right. \\ &\qquad \left.\times\delta\left[\left(\frac{1}{2}\frac{\partial^2 w^{(j)}}{\partial x^2}\right)\left(\frac{\partial w^{(j)}}{\partial x}\right)^2+\frac{\partial^2 w^{(j)}}{\partial x^2}\right]\right\}\mathrm{d}x+\int_{l_1^{(j)}}^{l_2^{(j)}}\beta_{33}A_p^{(j)}D_{3(bot)}^{(j)}\delta D_{3(bot)}^{(j)}\,\mathrm{d}x \\ &\quad -\int_{l_1^{(j)}}^{l_2^{(j)}}\left(\frac{1}{2}\left(t_s^{(j)}+t_p^{(j)}\right)h_{31}A_p^{(j)}\right)\left\{\left[\left(\frac{1}{2}\frac{\partial^2 w^{(j)}}{\partial x^2}\right)\left(\frac{\partial w^{(j)}}{\partial x}\right)^2+\frac{\partial^2 w^{(j)}}{\partial x^2}\right]\delta D_{3(bot)}^{(j)}\right. \\ &\qquad \left.+D_{3(bot)}^{(j)}\delta\left[\left(\frac{1}{2}\frac{\partial^2 w^{(j)}}{\partial x^2}\right)\left(\frac{\partial w^{(j)}}{\partial x}\right)^2+\frac{\partial^2 w^{(j)}}{\partial x^2}\right]\right\}\mathrm{d}x.\end{aligned} \tag{10}$$

Using the generalised Hamilton's principle [29, 30],

$$\int_{t_1}^{t_2}\left[\delta KE^{(j)}-\left(\delta\Pi_s^{(j)}+\delta\Pi_{pz(top)}^{(j)}+\delta\Pi_{pz(bot)}^{(j)}\right)+\delta W_e^{(j)}+\delta W_D^{(j)}\right]\mathrm{d}t=0, \tag{11}$$

the coupled equations of motion of the *j*th PB can be obtained as

$$
\begin{aligned}
&m^{(j)}(x)\frac{\partial^2 w^{(j)}}{\partial t^2}+\frac{\partial}{\partial x}\left\{\frac{\partial w^{(j)}}{\partial x}\int_L^x m^{(j)}(x)\left[\int_0^x\left(\frac{\partial^3 w^{(j)}}{\partial x\partial t^2}\frac{\partial w^{(j)}}{\partial x}+\left(\frac{\partial^2 w^{(j)}}{\partial x\partial t}\right)^2\right)\mathrm{d}x\right]\mathrm{d}x\right\}\\
&+\frac{\partial}{\partial x}\left\{\frac{1}{2}\left(\frac{\partial w^{(j)}}{\partial x}\right)^2\frac{\partial}{\partial x}\left[C^{(j)}(x)\left(\frac{\partial^2 w^{(j)}}{\partial x^2}\right)\right]+\frac{\partial}{\partial x}\left[C^{(j)}(x)\left(\frac{\partial^2 w^{(j)}}{\partial x^2}+\left(\frac{1}{2}\frac{\partial^2 w^{(j)}}{\partial x^2}\right)\left(\frac{\partial w^{(j)}}{\partial x}\right)^2\right)\right]\right\}\\
&+\frac{\partial}{\partial x}\left[\frac{\partial}{\partial x}\left(h^{(j)}(x)D_{3(top)}^{(j)}-h^{(j)}(x)D_{3(bot)}^{(j)}\right)\left(1+\frac{1}{2}\left(\frac{\partial w^{(j)}}{\partial x}\right)^2\right)\right]\\
&-m^{(j)}(x)a_b\sin(\omega_b t)+c_d^{(j)}(x)\left(\frac{a_b}{\omega_b}\cos(\omega_b t)+\frac{\partial w^{(j)}}{\partial t}\right)=0,
\end{aligned}
\tag{12}
$$

$$
\beta^{(j)}(x)D_{3(top)}^{(j)}+b^{(j)}V_{top}^{(j)}(t)G^{(j)}(x)+h^{(j)}(x)\left(\frac{1}{2}\left(\frac{\partial w^{(j)}}{\partial x}\right)^2+1\right)\frac{\partial^2 w^{(j)}}{\partial x^2}=0,
\tag{13}
$$

$$
\beta^{(j)}(x)D_{3(bot)}^{(j)}-b^{(j)}V_{bot}^{(j)}(t)G^{(j)}(x)-h^{(j)}(x)\left(\frac{1}{2}\left(\frac{\partial w^{(j)}}{\partial x}\right)^2+1\right)\frac{\partial^2 w^{(j)}}{\partial x^2}=0,
\tag{14}
$$

in which

$$
\begin{aligned}
&C^{(j)}(x)=E_s I_s^{(j)}+2\left\{\frac{1}{3}c_{11}b^{(j)}\left[\left(t_p^{(j)}\right)^3+3\left(t_p^{(j)}\right)^2\left(\frac{t_s^{(j)}}{2}\right)+3t_p^{(j)}\left(\frac{t_s^{(j)}}{2}\right)^2\right]\right\}G^{(j)}(x),\\
&h^{(j)}(x)=h_{31}A_p^{(j)}\left[\frac{1}{2}\left(t_s^{(j)}+t_p^{(j)}\right)\right]G^{(j)}(x),\\
&\beta^{(j)}(x)=A_p^{(j)}\beta_{33}G^{(j)}(x),\\
&a_b=z_b\omega_b^2.
\end{aligned}
\tag{15}
$$

Obtaining the expressions for $D_{3(top)}^{(j)}$ and $D_{3(bot)}^{(j)}$ using Eqs. (13) and (14) and substituting into Eq. (12) gives

$$
\begin{aligned}
&m^{(j)}(x)\frac{\partial^2 w^{(j)}}{\partial t^2}+\frac{\partial}{\partial x}\left\{\left(\frac{\partial w^{(j)}}{\partial x}\right)\int_L^x m^{(j)}(x)\left[\int_0^x\left(\frac{\partial w^{(j)}}{\partial x}\frac{\partial^3 w^{(j)}}{\partial x\partial t^2}+\left(\frac{\partial^2 w^{(j)}}{\partial x\partial t}\right)^2\right)\mathrm{d}x\right]\mathrm{d}x\right\}\\
&+\frac{\partial}{\partial x}\left\{\frac{1}{2}\frac{\partial}{\partial x}\left[F^{(j)}(x)\left(\frac{\partial^2 w^{(j)}}{\partial x^2}\right)\right]\left(\frac{\partial w^{(j)}}{\partial x}\right)^2+\frac{\partial}{\partial x}\left[F^{(j)}(x)\left(\frac{\partial^2 w^{(j)}}{\partial x^2}+\frac{1}{2}\left(\frac{\partial w^{(j)}}{\partial x}\right)^2\frac{\partial^2 w^{(j)}}{\partial x^2}\right)\right]\right\}\\
&-\frac{\partial}{\partial x}\left\{\left(\frac{1}{2}\left(\frac{\partial w^{(j)}}{\partial x}\right)^2+1\right)\frac{\partial}{\partial x}\left[\left(V_{(top)}^{(j)}(t)+V_{(bot)}^{(j)}(t)\right)\frac{b^{(j)}G^{(j)}(x)h^{(j)}(x)}{\beta^{(j)}(x)}\right]\right\}\\
&-m^{(j)}(x)a_b\sin(\omega_b t)+c_d^{(j)}(x)\left(\frac{a_b}{\omega_b}\cos(\omega_b t)+\frac{\partial w^{(j)}}{\partial t}\right)=0,
\end{aligned}
\tag{16}
$$

in which

$$
F^{(j)}(x)=C^{(j)}(x)-\frac{2h^{(j)}(x)^2}{\beta^{(j)}(x)}. \tag{17}
$$

Next, the electrical circuit equation for the *j*th piezoelectric bimorph is obtained. To this end, the electric current generated can be expressed as

$$
i_{top}^{(j)}(t)=\frac{\partial}{\partial t}\left[\int_{A_{el(top)}^{(j)}}\left(\mathbf{D}_{top}^{(j)}.\mathbf{n}\right)\mathrm{d}A\right],\qquad i_{bot}^{(j)}(t)=\frac{\partial}{\partial t}\left[\int_{A_{el(bot)}^{(j)}}\left(\mathbf{D}_{bot}^{(j)}.\mathbf{n}\right)\mathrm{d}A\right], \tag{18}
$$

where A_{el} is the electrode surface area, **n** is the surface normal unit vector, and **D** is the vector of electric displacement.

For parallel-connection piezoelectric layers in a bimorph one can obtain

$$
\begin{aligned}
&V_{(top)}^{(j)}(t)=V_{(bot)}^{(j)}(t)=V^{(j)}(t),\\
&i_{top}^{(j)}(t)+i_{bot}^{(j)}(t)=V^{(j)}(t)/R_l=I_p^{(j)},
\end{aligned}
\tag{19}
$$

in which R_l denotes the load resistance and $I_p^{(j)}$ denotes the current passing through the *j*th piezoelectric bimorph.

Using Eqs. (13), (14), (18), and (19) one can obtain the following electrical circuit equation for a piezoelectric bimorph with parallel connection

$$C_p^{(j)}\frac{\mathrm{d}}{\mathrm{d}t}V^{(j)}(t)+\frac{I_p^{(j)}}{2}=\tilde{i}_{cs}^{(j)}, \tag{20}$$

in which $C_p^{(j)}$ and $\tilde{i}_{cs}^{(j)}$ are the capacitance and current source of the *j*th piezoelectric bimorph given by

$$C_p^{(j)}=\frac{b^{(j)}L_p^{(i)}}{t_p^{(j)}\beta_{33}},\quad \tilde{i}_{cs}^{(j)}=-b^{(j)}\left[\frac{1}{2}\left(t_s^{(j)}+t_p^{(j)}\right)\right]\frac{h_{31}}{\beta_{33}}\int_{l_1^{(j)}}^{l_2^{(j)}}\frac{\partial}{\partial t}\left(\frac{\partial^2 w^{(j)}}{\partial x^2}+\frac{1}{2}\left(\frac{\partial w^{(j)}}{\partial x}\right)^2\frac{\partial^2 w^{(j)}}{\partial x^2}\right)\mathrm{d}x. \tag{21}$$

For series-connection piezoelectric layers in a bimorph

$$\begin{aligned}&V_{(top)}^{(j)}(t)+V_{(bot)}^{(j)}(t)=V^{(j)}(t),\\ &i_{top}^{(j)}(t)=i_{bot}^{(j)}(t)=V^{(j)}(t)/R_l=I_p^{(j)},\end{aligned} \tag{22}$$

which together with Eqs. (13), (14), and (18) leads to

$$C_p^{(j)}\frac{\mathrm{d}}{\mathrm{d}t}V^{(j)}(t)+2I_p^{(j)}=2\tilde{i}_{cs}^{(j)}. \tag{23}$$

Hence, the general form of the nonlinear and coupled equations of the *j*th piezoelectric bimorph are given by

$$C_p^{(j)}\frac{\mathrm{d}}{\mathrm{d}t}V^{(j)}(t)+\alpha_1 I_p^{(j)}=\alpha_2\tilde{i}_{cs}^{(j)}, \tag{24}$$

$$\begin{aligned}&m^{(j)}(x)\frac{\partial^2 w^{(j)}}{\partial t^2}+\frac{\partial}{\partial x}\left\{\left(\frac{\partial w^{(j)}}{\partial x}\right)\int_L^x m^{(j)}(x)\left[\int_0^x\left(\frac{\partial w^{(j)}}{\partial x}\frac{\partial^3 w^{(j)}}{\partial x\partial t^2}+\left(\frac{\partial^2 w^{(j)}}{\partial x\partial t}\right)^2\right)\mathrm{d}x\right]\mathrm{d}x\right\}\\ &+\frac{\partial}{\partial x}\left\{\frac{1}{2}\frac{\partial}{\partial x}\left[F^{(j)}(x)\left(\frac{\partial^2 w^{(j)}}{\partial x^2}\right)\right]\left(\frac{\partial w^{(j)}}{\partial x}\right)^2+\frac{\partial}{\partial x}\left[F^{(j)}(x)\left(\frac{\partial^2 w^{(j)}}{\partial x^2}+\frac{1}{2}\left(\frac{\partial w^{(j)}}{\partial x}\right)^2\frac{\partial^2 w^{(j)}}{\partial x^2}\right)\right]\right\}\\ &-\frac{\partial}{\partial x}\left\{\left(\frac{1}{2}\left(\frac{\partial w^{(j)}}{\partial x}\right)^2+1\right)\frac{\partial}{\partial x}\left[\left(\alpha_3 V^{(j)}(t)\right)\frac{b^{(j)}G^{(j)}(x)h^{(j)}(x)}{\beta^{(j)}(x)}\right]\right\}\\ &-m^{(j)}(x)a_b\sin(\omega_b t)+c_d^{(j)}(x)\left(\frac{a_b}{\omega_b}\cos(\omega_b t)+\frac{\partial w^{(j)}}{\partial t}\right)=0,\end{aligned} \tag{25}$$

in which the values of α_1, α_2, and α_3 depend on the connection type of the piezoelectric layers in the bimorph, and given by

$$\begin{aligned}&\text{Parallel connection:} \quad \alpha_1 = \frac{1}{2},\ \alpha_2 = 1, \text{ and } \alpha_3 = 2,\\ &\text{Series connection:} \quad \alpha_1 = 2,\ \alpha_2 = 2, \text{ and } \alpha_3 = 1.\end{aligned} \tag{26}$$

2.2 Nonlinear electromechanical model for an array of PBs connected in parallel

In this section, the general nonlinear coupled equations for the *j*th piezoelectric bimorph are utilised to derive the complete nonlinear model for an array of PBs connected in parallel, i.e. the configurations shown in Figs. 2(c) and 2(d). For a parallel connection of an array of PBs, one can obtain

$$\begin{aligned}&V^{(1)} = V^{(2)} = \ldots = V^{(N)} = V,\\ &\sum_{j=1}^{N} I_p^{(j)} = \frac{V}{R_l}.\end{aligned} \tag{27}$$

The electrical circuit equations for such array are given by

$$\begin{aligned}&C_p^{(1)} \frac{\mathrm{d}}{\mathrm{d}t} V^{(1)}(t) + \alpha_1 I_p^{(1)} = \alpha_2 \tilde{i}_{cs}^{(1)},\\ &C_p^{(2)} \frac{\mathrm{d}}{\mathrm{d}t} V^{(2)}(t) + \alpha_1 I_p^{(2)} = \alpha_2 \tilde{i}_{cs}^{(2)},\\ &\qquad \vdots\\ &C_p^{(N)} \frac{\mathrm{d}}{\mathrm{d}t} V^{(N)}(t) + \alpha_1 I_p^{(N)} = \alpha_2 \tilde{i}_{cs}^{(N)}.\end{aligned} \tag{28}$$

Hence, the complete nonlinear coupled electromechanical model of an array of PBs connected in parallel can be obtained as

$$\left(\sum_{j=1}^{N} C_p^{(j)} \right) \frac{\mathrm{d}}{\mathrm{d}t} V(t) + \alpha_1 \frac{V(t)}{R_l} = \alpha_2 \sum_{j=1}^{N} \tilde{i}_{cs}^{(j)}, \tag{29}$$

$$
\begin{aligned}
&m^{(j)}(x)\frac{\partial^2 w^{(j)}}{\partial t^2}+\frac{\partial}{\partial x}\left\{\left(\frac{\partial w^{(j)}}{\partial x}\right)\int_L^x m^{(j)}(x)\left[\int_0^x\left(\frac{\partial w^{(j)}}{\partial x}\frac{\partial^3 w^{(j)}}{\partial x\partial t^2}+\left(\frac{\partial^2 w^{(j)}}{\partial x\partial t}\right)^2\right)\mathrm{d}x\right]\mathrm{d}x\right\}\\
&+\frac{\partial}{\partial x}\left\{\frac{1}{2}\frac{\partial}{\partial x}\left[F^{(j)}(x)\left(\frac{\partial^2 w^{(j)}}{\partial x^2}\right)\right]\left(\frac{\partial w^{(j)}}{\partial x}\right)^2+\frac{\partial}{\partial x}\left[F^{(j)}(x)\left(\frac{\partial^2 w^{(j)}}{\partial x^2}+\frac{1}{2}\left(\frac{\partial w^{(j)}}{\partial x}\right)^2\frac{\partial^2 w^{(j)}}{\partial x^2}\right)\right]\right\}\\
&-\frac{\partial}{\partial x}\left\{\left(\frac{1}{2}\left(\frac{\partial w^{(j)}}{\partial x}\right)^2+1\right)\frac{\partial}{\partial x}\left[\left(\alpha_3 V(t)\right)\frac{b^{(j)}G^{(j)}(x)h^{(j)}(x)}{\beta^{(j)}(x)}\right]\right\}\\
&-m^{(j)}(x)a_b\sin(\omega_b t)+c_d^{(j)}(x)\left(\frac{a_b}{\omega_b}\cos(\omega_b t)+\frac{\partial w^{(j)}}{\partial t}\right)=0, \qquad j=1,2,...,N,
\end{aligned}
\tag{30}
$$

in which the values of α_1, α_2, and α_3, as mentioned before, depend on the type of the connection of piezoelectric layers in each PB, as given in Eq. (26).

2.3 Nonlinear electromechanical model for an array of PBs connected in series

In this section, the complete nonlinear model for an array of PBs connected in series is derived for the two configurations shown in Figs. 2(a) and 2(b). For a series connection of an array of PBs, one can obtain

$$
\begin{aligned}
&\sum_{j=1}^{N}V^{(j)}=V,\\
&I_p^{(1)}=I_p^{(2)}=...=I_p^{(N)}=\frac{V}{R_l}=\frac{1}{R_l}\sum_{j=1}^{N}V^{(j)},
\end{aligned}
\tag{31}
$$

with the electrical circuit equations already given in Eq. (28). Hence, one can obtain the complete nonlinear electromechanical model for an array of PBs connected in series as

$$
\begin{aligned}
&C_p^{(1)}\frac{\mathrm{d}}{\mathrm{d}t}V^{(1)}(t)+\frac{\alpha_1}{R_l}\sum_{j=1}^{N}V^{(j)}=\alpha_2\tilde{i}_{cs}^{(1)},\\
&C_p^{(2)}\frac{\mathrm{d}}{\mathrm{d}t}V^{(2)}(t)+\frac{\alpha_1}{R_l}\sum_{j=1}^{N}V^{(j)}=\alpha_2\tilde{i}_{cs}^{(2)},\\
&\quad\vdots\\
&C_p^{(N)}\frac{\mathrm{d}}{\mathrm{d}t}V^{(N)}(t)+\frac{\alpha_1}{R_l}\sum_{j=1}^{N}V^{(j)}=\alpha_2\tilde{i}_{cs}^{(N)},
\end{aligned}
\tag{32}
$$

$$
\begin{aligned}
&m^{(j)}(x)\frac{\partial^2 w^{(j)}}{\partial t^2}+\frac{\partial}{\partial x}\left\{\left(\frac{\partial w^{(j)}}{\partial x}\right)\int_L^x m^{(j)}(x)\left[\int_0^x\left(\frac{\partial w^{(j)}}{\partial x}\frac{\partial^3 w^{(j)}}{\partial x\partial t^2}+\left(\frac{\partial^2 w^{(j)}}{\partial x\partial t}\right)^2\right)\mathrm{d}x\right]\mathrm{d}x\right\}\\
&+\frac{\partial}{\partial x}\left\{\frac{1}{2}\frac{\partial}{\partial x}\left[F^{(j)}(x)\left(\frac{\partial^2 w^{(j)}}{\partial x^2}\right)\right]\left(\frac{\partial w^{(j)}}{\partial x}\right)^2+\frac{\partial}{\partial x}\left[F^{(j)}(x)\left(\frac{\partial^2 w^{(j)}}{\partial x^2}+\frac{1}{2}\left(\frac{\partial w^{(j)}}{\partial x}\right)^2\frac{\partial^2 w^{(j)}}{\partial x^2}\right)\right]\right\}\\
&-\frac{\partial}{\partial x}\left\{\left(\frac{1}{2}\left(\frac{\partial w^{(j)}}{\partial x}\right)^2+1\right)\frac{\partial}{\partial x}\left[\left(\alpha_3 V^{(j)}(t)\right)\frac{b^{(j)}G^{(j)}(x)h^{(j)}(x)}{\beta^{(j)}(x)}\right]\right\}\\
&-m^{(j)}(x)a_b\sin(\omega_b t)+c_d^{(j)}(x)\left(\frac{a_b}{\omega_b}\cos(\omega_b t)+\frac{\partial w^{(j)}}{\partial t}\right)=0, \qquad j=1,2,\ldots,N.
\end{aligned}
\tag{33}
$$

3. Discretisation

The nonlinear model developed for an array of PBs connected in *parallel* consists of one ordinary differential equation (ODE), i.e. the electrical circuit equation, and one partial differential equation (PDE), i.e. the continuous equation of motion of the cantilever bimorph. The model developed for an array of PBs connected in *series* consists of *N* ODEs and one PDE. To be able to solve these nonlinear models numerically, the PDEs in both models should be discretised into a set of ODEs. Hence, transverse motion for the *j*th PB is defined as a series expansion [31, 32] of suitable shape functions $\Lambda_k(x)$ multiplied by time-dependent coordinates $p_k^{(j)}(t)$ as [33, 34]

$$w^{(j)}(x,t)=\sum_{k=1}^{M}\Lambda_k(x)p_k^{(j)}(t), \tag{34}$$

where

$$\begin{aligned}\Lambda_k(x)&=\left[\cosh\left(\frac{\theta_k x}{L}\right)-\psi_k\sinh\left(\frac{\theta_k x}{L}\right)\right]-\left[\cos\left(\frac{\theta_k x}{L}\right)-\psi_k\sin\left(\frac{\theta_k x}{L}\right)\right],\\ \psi_k&=\left(\sinh(\theta_k)+\sin(\theta_k)\right)^{-1}\left(\cosh(\theta_k)+\cos(\theta_k)\right),\end{aligned} \tag{35}$$

in which θ_k is *k*th root the equation $1+\cos\theta\cosh\theta=0$. The defined expression for transverse motion is first substituted into current source terms to perform the spatial integration and to obtain the electrical circuit ODEs. The continuous cantilever PDE is discretised using the Galerkin method [35, 36] based on the transverse motion defined in Eq. (34). Three vibration modes are retained for the transverse motion of each piezoelectric bimorph (i.e. *M*=3). Hence, the dimension of the discretised model for an array of *N* PBs connected in *parallel* is 3*N*+1 while that for an array of *N* PBs connected in *series* is 3*N*+*N* = 4*N*. These discretised sets of equations, consisting of geometric and inertial nonlinearities, are solved numerically through use of an efficient and highly optimised continuation method [37-41].

4. Results and discussions

The electromechanical behaviour of the energy harvester is studied in this section for various cases. For all the numerical results shown in this section, the piezoelectric and substrate lengths are the same and equal to 80 mm. The properties of the piezoelectric bimorph are given in Table 1. Substitution of piezoelectric constants given in Table 1 into Eq.

(4) gives c_{11}=68.81 GPa, h_{31}= - 579.76 MV/m, and β_{33}=38.03 Mm/F. Throughout this section, ζ is set to 0.017 and the base acceleration is set to 9.81 m/s^2. ζ is the damping ratio which is related to the mass-normalised damping coefficient $c_{d(n)}^{(j)}$ through $c_{d(n)}^{(j)} = 2\zeta\omega_1^{(j)}$, with $\omega_1^{(j)}$ being the first natural frequency of the *j*th piezoelectric bimorph. For the cases examined in this section with L_p=L, one can obtain $c_{d(n)}^{(j)} = c_d\left(1+2A_p^{(j)}/A_s^{(j)}\right)\Big/\left(\rho_s A_s^{(j)} + 2\rho_p A_p^{(j)} + 4M_p^{(j)}\right)$. Additionally, it should be noted that the piezoelectric layers in each bimorph are assumed to be connected in parallel for all cases. The numerical results and discussions are structured as follows: in Section 4.1, a single PB is examined to study the effect of layers' thicknesses and widths on the power output of the energy harvester. Section 4.2 studies the response of an array of 4PBs connected in parallel and series and examines different designs. Section 4.3 studies the effect of the natural frequency tuning in PBs on the energy harvester operating resonance region. The effect of the number of PBs in an array is investigated in Section 4.4. Finally in Section 4.5, design considerations are suggested to enhance the broadband energy harvesting efficiency of an array of PBs.

4.1 Single piezoelectric bimorph harvester

The section examines the effect of the piezoelectric and substrate thicknesses and widths on the power output of a single PB. The goal of this section is to gain an understanding on the behaviour of a single-PB energy harvester before analysing a multi-PB one.

Figure 3 shows the power output of a single-PB energy harvester for various substrate thicknesses when *b*=15 mm; for all cases, the piezoelectric thickness is obtained

such that the mass of the PB remains constant and equal to 8 g; the proof mass is equal to 8 g as well for all cases. Hence, the total mass of the PB for all cases is equal to 16 g. The reason for keeping the mass constant is to obtain the optimum thicknesses for substrate and piezoelectric layers which result in maximum power output. It is seen in Fig. 3 that, as the substrate thickness is decreased from t_s=0.6 mm, the power output increases until reaching t_s=0.4 mm; the power output decreases with further decreasing the substrate thickness. Conducting a parametric analysis in the vicinity of t_s=0.4 mm reveals that the optimum thickness for substrate and piezoelectric layers are: t_s=0.42 mm and t_p=0.21 mm. These thicknesses are used throughout the rest of Section 4.

The effect of the width of the cantilever PB on power outputs is shown in Fig. 4; for all cases, the base frequency ω_b is set to 1.01 ω_1 in order to obtain the maximum possible power output, with ω_1 being the fundamental short-circuit transverse natural frequency. For each case, the ratio of tip mass to PB mass is equal to 1. As seen in Fig. 4, $P_{\max}$ increases with increasing width of the PB. Additionally, as the width is increased, the maximum power output occurs at smaller values of load resistance. To better highlight the influences of PB's width on power output, Fig. 5 is constructed showing the frequency responses for b=10 mm, 20 mm, and 30 mm; for each case, the load resistance is set to its optimum value. As seen, the whole multi-valued region of the power output becomes larger as a result of increasing the PB's width. This finding will be used later for efficient design of an array of PBs.

4.2 An array of 4 PBs in parallel/series

This section examines the energy harvesting capabilities of arrays of 4 PBs in

parallel/series for different sets of parameters; for all PBs b=15 mm. The main reason for using arrays of PBs for energy harvesting is to increase the resonance bandwidth and to harvest energy in a wide range of frequencies. Hence, PBs in an array must have different natural frequencies and hence different resonance regions to ensure broadband energy harvesting. The most efficient and practical method to create a difference in the natural frequencies of PBs in an array is by modifying the proof mass. In fact, in this section, the thicknesses and lengths of all PBs are the same. For each case, the proof mass is chosen such that to create the desired difference in the PBs' natural frequencies.

Figures 6 and 8 show the power and voltage outputs of an array of 4 PBs connected in parallel and series, respectively, for several values of load resistance. Since the thicknesses and lengths of all PBs are the same, the proof masses are chosen in a way to create ~1 Hz difference in short-circuit natural frequencies of the PBs. In particular, for both cases of Figs. 6 and 8, the proof masses are set to $M_p^{(1)}$ = 6.9 g, $M_p^{(2)}$ = 7.5 g, $M_p^{(3)}$ = 8.2 g, and $M_p^{(4)}$ = 9.0 g.

Figure 6 shows the effect of load resistance on an energy harvesting array of 4 PBs connected in parallel. It is seen that as R_l is increased from 1 kΩ to 3 kΩ, the power output increases in the whole multi-frequency resonance region. By further increasing the R_l from 3 kΩ to 5 kΩ, the power output increases at larger base frequencies while it decreases at smaller base frequencies. A similar behaviour of observed as R_l is increased from 5 kΩ to 7 kΩ; however, for this cases it is visible that the power output reductions at smaller frequencies are larger than those gained at higher frequencies. A more detailed parametric analysis around R_l = 5 kΩ reveals that the optimum load resistance for this array configuration is R_l = 4 kΩ. Figure 7 shows the maximum tip transverse displacement of the

cantilever PBs connected in parallel when R_l = 4 kΩ. As seen, the tip displacement is slightly larger for the two PBs at the ends of the resonance frequency spectrum.

The effect of load resistance on an array of 4 PBs connected in series is depicted in Fig. 8 The first thing to notice is that the values of load resistance for optimum power output for this case are much larger than those for the previous case, i.e. parallel-type connection. The other major difference of the series connection with the parallel one is that, as a result of increasing the load resistance, the output power increases at smaller base frequencies and it decreases at larger base frequencies which is the exact opposite of the case of PBs connected in parallel. Performing a more detailed parametric analysis around R_l = 100 kΩ reveals that the optimum load resistance for this series array configuration is R_l = 90 kΩ. A comparison between the two cases show the optimum load resistance for parallel is around 4% of that for series. To better depict the differences between the parallel and series connections of an array of 4 PBs, Fig. 9 is constructed showing the maximum power output of the two cases at their optimum load resistance.

4.3 Tuning the operating resonance region

As mentioned in Section 4.2, in this study the desired broadband energy harvesting for an array of PBs is achieved through appropriate selection of the proof masses. The proof masses are not only used to tune the energy-harvester operation region, but also to determine how close the resonance region of one PB is to that of the neighbouring PBs. Modifying the proof masses for tuning the design of an array of PBs is much more practical and efficient than modifying the thicknesses of the PBs. In this section, an energy harvesting

device consisting of 8 PBs connected in parallel is considered; for all PBs *b*=15 mm. Figure 10 shows four different designs for such energy harvesting device. The only difference between the designs is in the selection of proof masses. In particular, the proof masses are selected such that the short-circuit fundamental natural frequencies of the PBs are 1.5 Hz apart for design 1, 1.0 Hz apart for design 2, 0.75 Hz apart for design 3, and 0.5 Hz apart for design 4. It should be noted that mass of all the designs are almost the same. It is seen in Fig. 10 that, as the difference between PBs' natural frequencies is increased, the operating bandwidth becomes wider; however, the power output level decreases significantly. For instance, design 1 with PBs' natural frequencies being 1.5 Hz apart has the widest bandwidth, but the lowest power output level within the operating resonance region among all the designs. Hence, a larger difference between the PBs' natural frequencies causes a larger bandwidth with smaller power threshold, while a smaller difference between the PBs' natural frequencies results in a smaller bandwidth with much larger power threshold.

4.4 Effect of the number of PBs in an array

This section examines the effect of the number of PBs in an energy harvesting device on the power and voltage outputs. It is assumed that for all cases PBs are connected in parallel. The width of each PB is set to 15 mm; all PBs dimensions are the same, with the only difference between them being the proof mass. The effect of the number of PBs is examined on two energy harvesting devices, one with PBs' natural frequencies being 1 Hz apart, as shown in Fig. 11, and the other with PBs' natural frequencies being 0.5 Hz apart, as depicted in Fig. 12. The frequency responses for each case are obtained for 1 PB, 2 PBs, 4

PBs, and 8 PBs, with the load resistance being set to its optimum value of 11.5 kΩ for 1 PB, 7.0 kΩ for 2 PBs, 4.5 kΩ for 4 PBs, and 2.5 kΩ for 8 PBs.

For the energy harvesting device examined in Fig. 11, the proof masses are selected such that the PBs' natural frequencies are 1 Hz apart and that the total mass of each array is around N×16 g, with N being the number of PBs in the array. As seen, the resonance operating bandwidth of the energy harvester can be effectively increased via increasing the number of PBs. A comparison between the operating bandwidth of a single PB, an array of 4 PBs, and an array of 8 PBs based on different power output thresholds is given in Table 2. As seen in the table, the percentage increase in the bandwidth is higher at larger power thresholds. It is seen that for a power threshold of 0.01 W, the energy harvester array with 8 PBs reaches a bandwidth of more than 14 Hz, which is a significantly large bandwidth for its operating frequency.

Figure 12 shows the effect of number of PBs on the power and voltage outputs of an energy harvesting device with PBs' natural frequencies being 0.5 Hz apart. Similar to the previous case, the total mass of each array is around N×16 g, with N being the number of PBs in the array. As seen, compared to the previous case, there is a smaller increase in the resonance bandwidth with increasing number of PBs. However, for this case, the power output level in the operating resonance region is much higher than that of the case of Fig. 11.

4.5 Design enhancements for improving the power output of an array of PBs

It is seen that for both energy harvesting devices of Figs. 11 and 12, when the

number of PBs is increased to 8, there is a power drop in the operating resonance region. In fact, this is one of the drawbacks of a design with multiple PBs having the same dimensions. It was shown in Section 4.1 that the power output of a PB can be efficiently increased by increasing its width. In this section, the designs of the two energy harvesting devices of Figs. 11 and 12 for the case of 8 PBs are modified while keeping the total mass constant in order to improve the power output efficiency in the operating resonance region.

Starting with the energy harvesting device of Fig. 11, i.e. the one with PBs' natural frequencies being 1 Hz apart, it is seen that there is a significant power drop in the middle of the operating region while the power output is maximised near the two ends. In this "initial design", all PBs have the same width of 15 mm. In order to improve this design, the widths of the PBs should be modified such that the PBs in the middle generate more power compared to the ones in the two ends. A detailed parametric analysis is conducted on the width of the PBs with the goal of increasing the power output local minima in the resonance region and an "enhanced design" is achieved through a specific selection of widths for the PBs, as detailed in Table 3. The comparison between the two designs is shown in Fig. 13 for the energy harvesting device with PBs' natural frequencies being 1 Hz apart. As seen, the proposed enhanced design does a much better job in producing consistent level of power output throughout the resonance region. Comparing the results of the two designs reveal that the initial design with the same widths for all PBs reaches a minimum power output of 0.0286 W in the resonance region while the enhanced design reaches a minimum of 0.0378 W, i.e. 32 % increase compared to the initial design. The comparison between the initial and enhanced designs for the energy harvester array of Fig. 12, with PBs' natural frequencies being 0.5 Hz apart, is show in Fig. 14. As seen, the enhanced design outputs generally higher

power levels in the operating resonance region. Hence, the results presented in this section show that for optimum design of an array of PBs connected in parallel, the widths of the PBs in the middle should be generally larger than those of the PBs near the ends.

5. Conclusions

The nonlinear electromechanical behaviours of energy harvesting devices consisting of multiple piezoelectric bimorphs were investigated numerically. Complete nonlinear models were proposed for parallel and series connections of multiple piezoelectric bimorphs. Utilising the piezoelectric and beam constitutive equations and the Galerkin method, the nonlinear multi-modal discretised models of the energy harvesting arrays of PBs were developed. These models were solved numerically via use of a highly optimised continuation code.

Examining the electromechanical response of a single piezoelectric bimorph revealed that the power output is maximised when the substrate thickness is twice each piezoelectric layer's thickness. Additionally it was shown that as the width of the bimorph is increased, the maximum power output increases accordingly, while the optimum load resistance corresponding to maximum power decreases.

Examining the behaviour of an array of 4 PBs connected in parallel and series revealed that the optimum load resistance for parallel is around 4% of that for series, which is very important from design perspective. It was shown that for the energy harvesting device with parallel connection of PBs, the maximum power output tends to occur near the

highest resonance frequency while for the one with series connection of PBs that happens near the lowest resonance frequency.

It was shown that the proof masses can be employed effectively to tune energy harvester's resonance region and to determine the difference between resonance frequencies of the PBs. It was concluded that as the difference between PBs' natural frequencies becomes smaller, the energy harvester produces much larger power outputs at the cost of reduced bandwidth. Examining the effect of the number of PBs in an array showed that the operating bandwidth can be efficiently increased by increasing the number of PBs. In fact, based on the power threshold of 0.01 W, an energy harvesting array of 8 PBs reached a bandwidth of 14 Hz in a relatively low operating frequency range, i.e. 20-34 Hz. Additionally, it was shown that the operating bandwidth could be increased by more than 500% using 8 PBs instead of 1 PB.

Finally, it was shown that in multi-PB energy harvesting devices, the power output tend to drop in the middle of the resonance region. In fact, the results indicated that this power drop becomes larger as the number of PBs is increased. Design enhancements were introduced to reduce this power drop as much as possible and to enhance the efficiency of the energy harvesting device.

Appendix A. Significance of nonlinear modelling

This appendix conducts a comparison between nonlinear and linear models of a piezoelectric bimorph energy harvester. The analysis is carried out for a single PB of L=80 mm, R_l=133.5 kΩ, t_s= t_p=0.2 mm, l_1=0, l_2=0.35L, M_p=8.2 g, and a_b=9.81 m/s^2. A comparison is given in Fig. 15; the complete nonlinear model developed in this study, which takes into account both inertial and geometric nonlinearities, anticipates a hardening-type nonlinear response and much smaller peak transverse amplitude compared to linear model. The figure also shows that accounting for only one source of nonlinearity, geometric or inertial, leads to very wrong results. The figure signifies the importance of retaining all sources of nonlinearities while examining piezoelectric bimorph energy harvesters.

Appendix B. Verification

The section examines the accuracy of the proposed model via comparing it to experimental results from Ref. [21]. In particular, the voltage output obtained experimentally for a single piezoelectric bimorph in Ref. [21] is calculated using the proposed model by setting N=1. The PB's dimensions and properties are set to the values given in Ref. [21]; additionally, a_b=9.81 m/s^2, R_l=33 kΩ, M_p=0.012 kg, and ζ=0.027. It is important to note that since in Ref. [21] the width of the PB is very wide, i.e. almost 63% of the length, the plane strain elastic moduli are used for both substrate and piezoelectric, i.e. E_s and c_{11} are replaced by $E_s/(1-\nu_s^2)$ and $c_{11}/(1-\nu_p^2)$, respectively. Figure 16 shows the comparison between the voltage output frequency response obtained based on the proposed model (indicated by solid line) and that reported experimentally. As seen, the comparison shows excellent

agreement between the results of the present study and the experimental observations, verifying the accuracy of the proposed model.

References

[1] Yildirim, T., Ghayesh, M. H., Li, W., and Alici, G., 2017, "A review on performance enhancement techniques for ambient vibration energy harvesters," Renewable and Sustainable Energy Reviews, 71, pp. 435-449.
[2] Ali, S. F., and Adhikari, S., 2013, "Energy harvesting dynamic vibration absorbers," Journal of Applied Mechanics, Transactions ASME, 80(4).
[3] Boisseau, S., Despesse, G., and Seddik, B. A., 2013, "Nonlinear h-shaped springs to improve efficiency of vibration energy harvesters," Journal of Applied Mechanics, Transactions ASME, 80(6).
[4] Chen, L. Q., and Jiang, W. A., 2015, "Internal Resonance Energy Harvesting," Journal of Applied Mechanics, Transactions ASME, 82(3).
[5] Li, H., Wang, X., Zhu, F., Ning, X., Wang, H., Rogers, J. A., Zhang, Y., and Huang, Y., 2018, "Viscoelastic Characteristics of Mechanically Assembled Three-Dimensional Structures Formed by Compressive Buckling," Journal of Applied Mechanics, Transactions ASME, 85(12).
[6] Wu, Z., Harne, R. L., and Wang, K. W., 2014, "Energy harvester synthesis via coupled linear-bistable system with multistable dynamics," Journal of Applied Mechanics, Transactions ASME, 81(6).
[7] Zou, H. X., Zhang, W. M., Wei, K. X., Li, W. B., Peng, Z. K., and Meng, G., 2016, "A Compressive-Mode Wideband Vibration Energy Harvester Using a Combination of Bistable and Flextensional Mechanisms," Journal of Applied Mechanics, Transactions ASME, 83(12).
[8] Ghayesh, M. H., and Farokhi, H., 2015, "Chaotic motion of a parametrically excited microbeam," International Journal of Engineering Science, 96, pp. 34-45.
[9] Ghayesh, M. H., Farokhi, H., and Amabili, M., 2013, "Nonlinear behaviour of electrically actuated MEMS resonators," International Journal of Engineering Science, 71, pp. 137-155.
[10] Ghayesh, M. H., Farokhi, H., and Alici, G., 2016, "Size-dependent performance of microgyroscopes," International Journal of Engineering Science, 100, pp. 99-111.
[11] Gholipour, A., Farokhi, H., and Ghayesh, M. H., 2015, "In-plane and out-of-plane nonlinear size-dependent dynamics of microplates," Nonlinear Dynamics, 79(3), pp. 1771-1785.
[12] Abdelkareem, M. A. A., Xu, L., Ali, M. K. A., El-Daly, A. R. B. M., Hassan, M. A., Elagouz, A., and Bo, Y., 2019, "Analysis of the prospective vibrational energy harvesting of heavy-duty truck suspensions: A simulation approach," Energy, pp. 332-351.
[13] Fan, K., Cai, M., Liu, H., and Zhang, Y., 2019, "Capturing energy from ultra-low frequency vibrations and human motion through a monostable electromagnetic energy harvester," Energy, pp. 356-368.
[14] Tang, X., Zhang, D., Liu, T., Khajepour, A., Yu, H., and Wang, H., 2019, "Research on the energy control of a dual-motor hybrid vehicle during engine start-stop process," Energy, pp. 1181-1193.
[15] Dutoit, N. E., Wardle, B. L., and Kim, S.-G., 2005, "Design considerations for MEMS-scale piezoelectric mechanical vibration energy harvesters," Integrated ferroelectrics, 71(1), pp. 121-160.
[16] Sodano, H. A., Inman, D. J., and Park, G., 2005, "Comparison of Piezoelectric Energy Harvesting Devices for Recharging Batteries," Journal of Intelligent Material Systems and Structures, 16(10), pp. 799-807.
[17] Soliman, M., Abdel-Rahman, E., El-Saadany, E., and Mansour, R., 2008, "A wideband vibration-based energy harvester," Journal of Micromechanics and Microengineering, 18(11), p. 115021.
[18] Beeby, S. P., Torah, R., Tudor, M., Glynne-Jones, P., O'donnell, T., Saha, C., and Roy, S., 2007, "A micro electromagnetic generator for vibration energy harvesting," Journal of Micromechanics and microengineering, 17(7), p. 1257.
[19] Xue, H., Hu, Y., and Wang, Q.-M., 2008, "Broadband piezoelectric energy harvesting devices using multiple bimorphs with different operating frequencies," IEEE transactions on ultrasonics, ferroelectrics, and frequency control, 55(9), pp. 2104-2108.
[20] Mann, B. P., and Sims, N. D., 2009, "Energy harvesting from the nonlinear oscillations of magnetic levitation," Journal of Sound and Vibration, 319(1), pp. 515-530.

[21] Erturk, A., and Inman, D. J., 2009, "An experimentally validated bimorph cantilever model for piezoelectric energy harvesting from base excitations," Smart Materials and Structures, 18(2), p. 025009.
[22] Kim, M., Hoegen, M., Dugundji, J., and Wardle, B. L., 2010, "Modeling and experimental verification of proof mass effects on vibration energy harvester performance," Smart Materials and Structures, 19(4), p. 045023.
[23] Lumentut, M. F., Francis, L. A., and Howard, I. M., 2012, "Analytical techniques for broadband multielectromechanical piezoelectric bimorph beams with multifrequency power harvesting," IEEE transactions on ultrasonics, ferroelectrics, and frequency control, 59(11), pp. 2555-2568.
[24] Nguyen, S. D., and Halvorsen, E., 2011, "Nonlinear springs for bandwidth-tolerant vibration energy harvesting," Journal of Microelectromechanical Systems, 20(6), pp. 1225-1227.
[25] Firoozy, P., Khadem, S. E., and Pourkiaee, S. M., 2017, "Broadband energy harvesting using nonlinear vibrations of a magnetopiezoelastic cantilever beam," International Journal of Engineering Science, 111, pp. 113-133.
[26] Ju, S., Chae, S. H., Choi, Y., Lee, S., Lee, H. W., and Ji, C.-H., 2013, "A low frequency vibration energy harvester using magnetoelectric laminate composite," Smart Materials and Structures, 22(11), p. 115037.
[27] Zhao, L., and Yang, Y., 2018, "An impact-based broadband aeroelastic energy harvester for concurrent wind and base vibration energy harvesting," Applied Energy, 212, pp. 233-243.
[28] Jalili, N., 2009, Piezoelectric-based vibration control: from macro to micro/nano scale systems, Springer Science & Business Media.
[29] Ghayesh, M. H., Farokhi, H., and Amabili, M., 2013, "Nonlinear dynamics of a microscale beam based on the modified couple stress theory," Composites Part B: Engineering, 50, pp. 318-324.
[30] Ghayesh, M. H., Amabili, M., and Farokhi, H., 2013, "Three-dimensional nonlinear size-dependent behaviour of Timoshenko microbeams," International Journal of Engineering Science, 71, pp. 1-14.
[31] Ghayesh, M. H., Farokhi, H., and Amabili, M., 2014, "In-plane and out-of-plane motion characteristics of microbeams with modal interactions," Composites Part B: Engineering, 60, pp. 423-439.
[32] Farokhi, H., Ghayesh, M., and Amabili, M., 2013, "Nonlinear dynamics of a geometrically imperfect microbeam based on the modified couple stress theory," International Journal of Engineering Science, 68 pp. 11-23.
[33] Ghayesh, M. H., 2018, "Functionally graded microbeams: Simultaneous presence of imperfection and viscoelasticity," International Journal of Mechanical Sciences, 140, pp. 339-350.
[34] Ghayesh, M. H., 2018, "Dynamics of functionally graded viscoelastic microbeams," International Journal of Engineering Science, 124, pp. 115-131.
[35] Farokhi, H., and Ghayesh, M. H., 2015, "Thermo-mechanical dynamics of perfect and imperfect Timoshenko microbeams," International Journal of Engineering Science, 91, pp. 12-33.
[36] Ghayesh, M. H., Amabili, M., and Farokhi, H., 2013, "Nonlinear forced vibrations of a microbeam based on the strain gradient elasticity theory," International Journal of Engineering Science, 63, pp. 52-60.
[37] Mittelmann, H. D., and Roose, D., 1990, Continuation techniques and bifurcation problems, Springer.
[38] Allgower, E. L., and Georg, K., 2003, Introduction to Numerical Continuation Methods, Society for Industrial and Applied Mathematics.
[39] Nayfeh, A. H., and Balachandran, B., 2008, Applied nonlinear dynamics: analytical, computational, and experimental methods, John Wiley & Sons.
[40] Krauskopf, B., Osinga, H. M., and Galán-Vioque, J., 2007, Numerical continuation methods for dynamical systems, Springer.
[41] Wasserstrom, E., 1973, "Numerical solutions by the continuation method," SIAM Review, 15(1), pp. 89-119.

Table 1. Piezoelectric and substrate properties.

Properties	Piezoelectric (PZT-5H)	Properties	Substrate (brass)
ρ_p (kg/m^3)	7400	ρ_s (kg/m^3)	8490
s_{11} (pm^2/N)	16.4	E_s (GPa)	106
ξ_{33}/ξ_0 (ξ_0 = 8.8542 pF/m)	3400		
d_{31} (pm/V)	-250		

Table 2. Operating bandwidth of different energy harvesters of Fig. 11.

Power threshold (W)	Energy harvester operating bandwidth (Hz)				
	Single PB	Array of 4 PBs	% bandwidth gain compared to 1 PB	Array of 8 PBs	% bandwidth gain compared to 1 PB
0.025	1.98	6.25	316	10.27	519
0.020	2.40	6.88	287	11.02	459
0.015	2.96	7.81	264	12.15	410
0.010	3.85	9.37	243	14.11	366

Table 3. Width of the PBs for the two designs of Figs. 13 and 14.

	Width of each PB (mm)							
	$b^{(1)}$	$b^{(2)}$	$b^{(3)}$	$b^{(4)}$	$b^{(5)}$	$b^{(6)}$	$b^{(7)}$	$b^{(8)}$
Initial design	15	15	15	15	15	15	15	15
Enhanced design	9	13	16	18	19	18	16	11

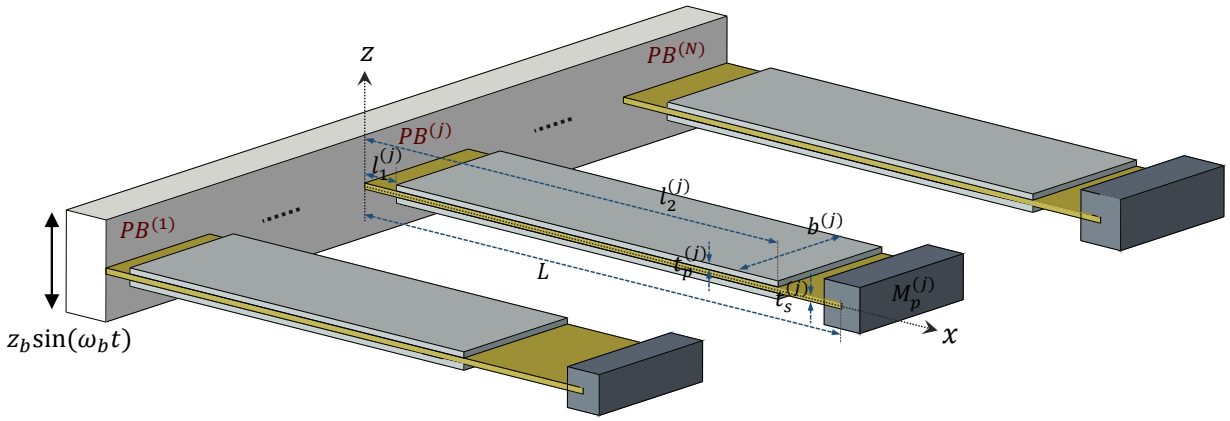

Fig.1. Schematic of an array of cantilever piezoelectric bimorph energy harvesters.

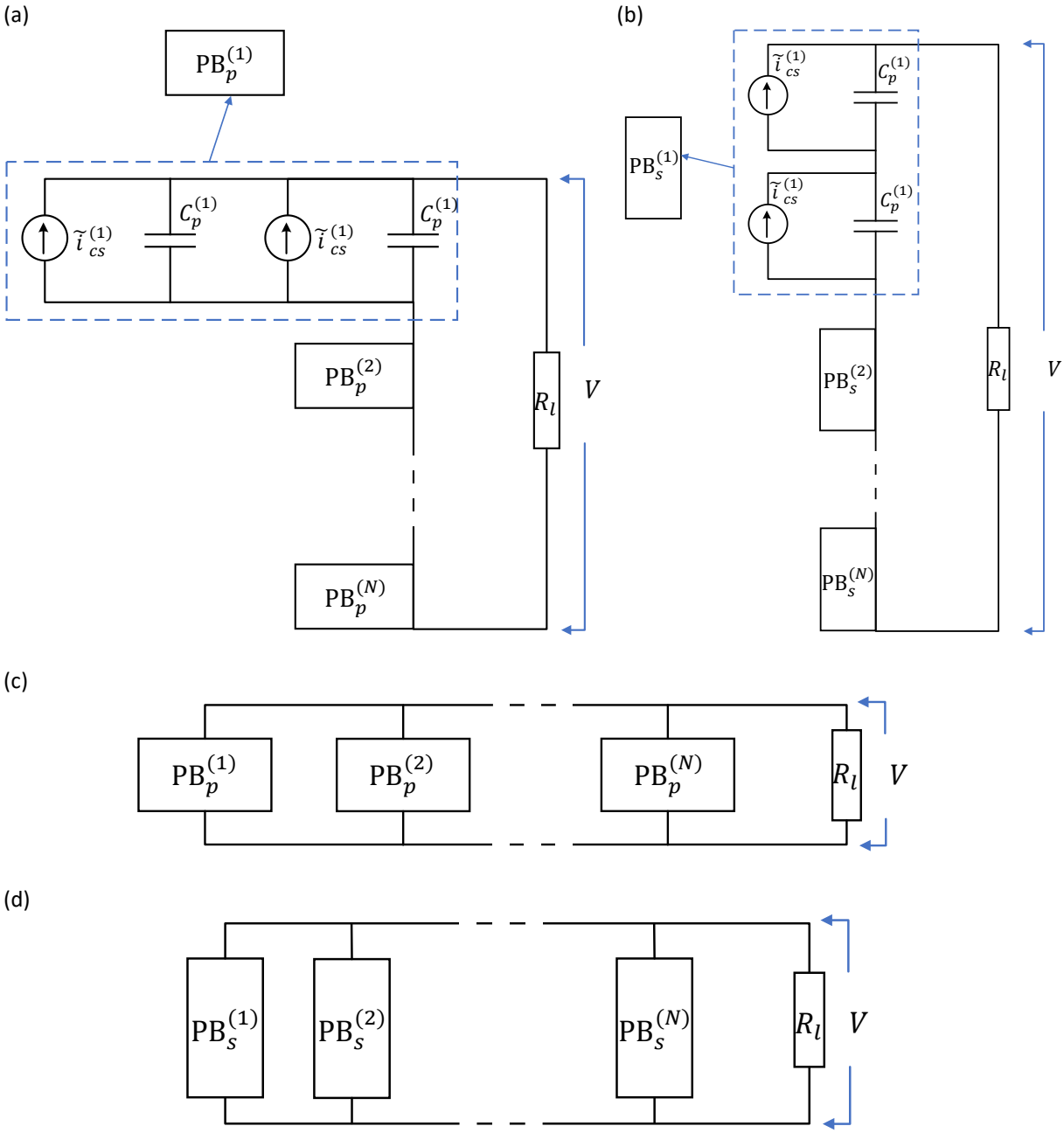

Fig.2. Electrical circuit diagrams of an array of: (a, b) parallel and serial PBs, respectively, connected in series, and (c, d) parallel and serial PBs, respectively, connected in parallel.

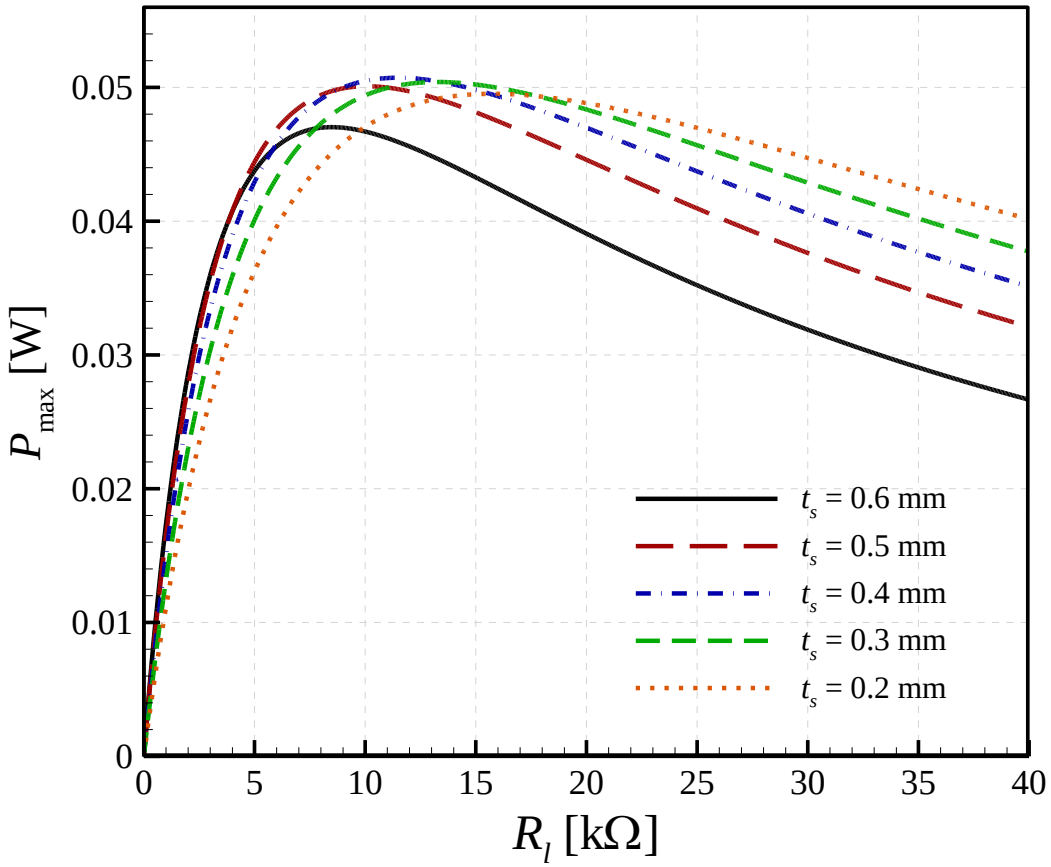

Fig.3. Maximum power output versus the load resistance for various substrate thicknesses. The piezoelectric thickness for each case is calculated such that the bimorph mass remains constant.

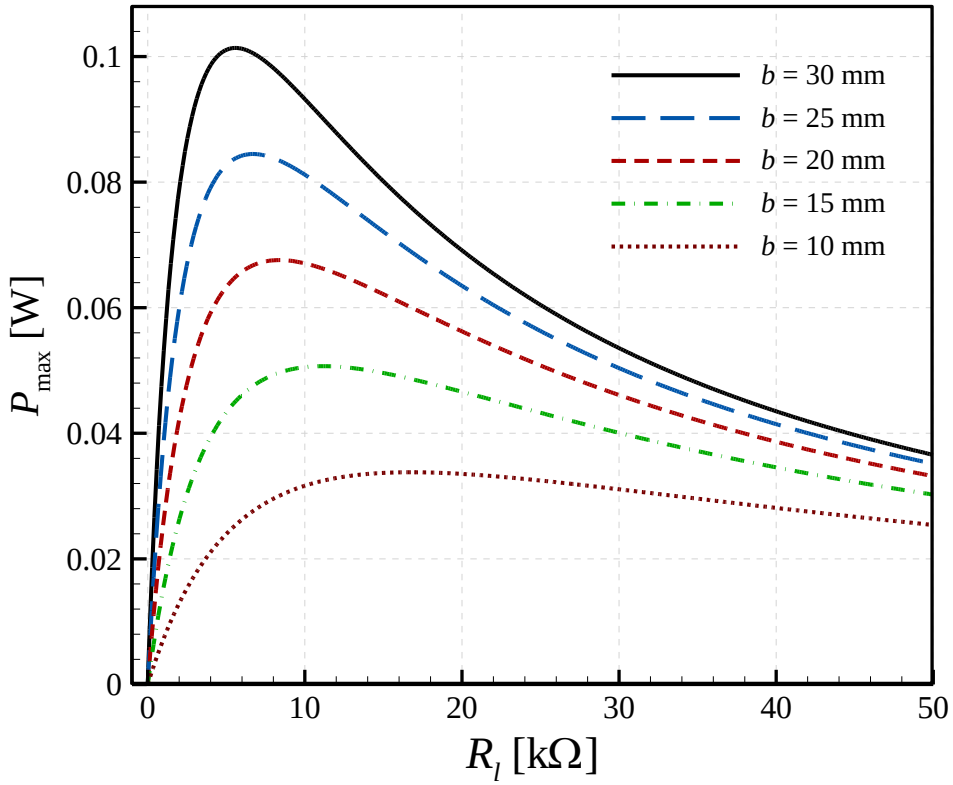

Fig.4. Effect of bimorph width on maximum power output.

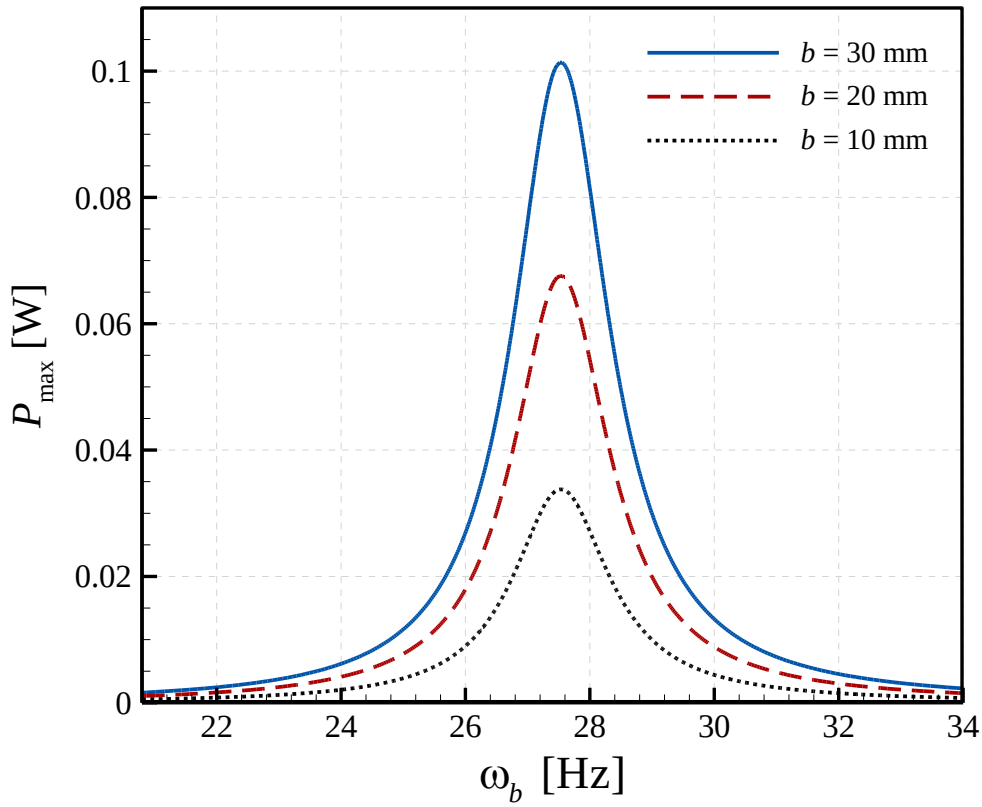

Fig.5. Effect of bimorph width on maximum power output frequency response. R_l is set to its optimum value for each case.

(a)

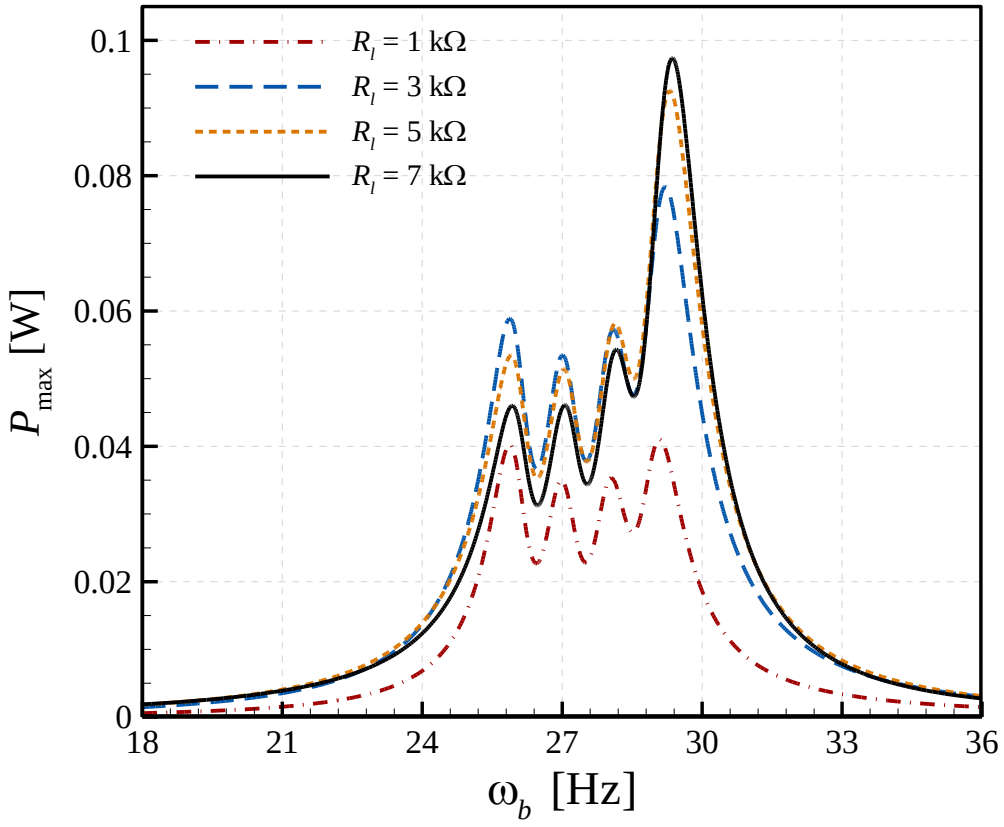

(b)

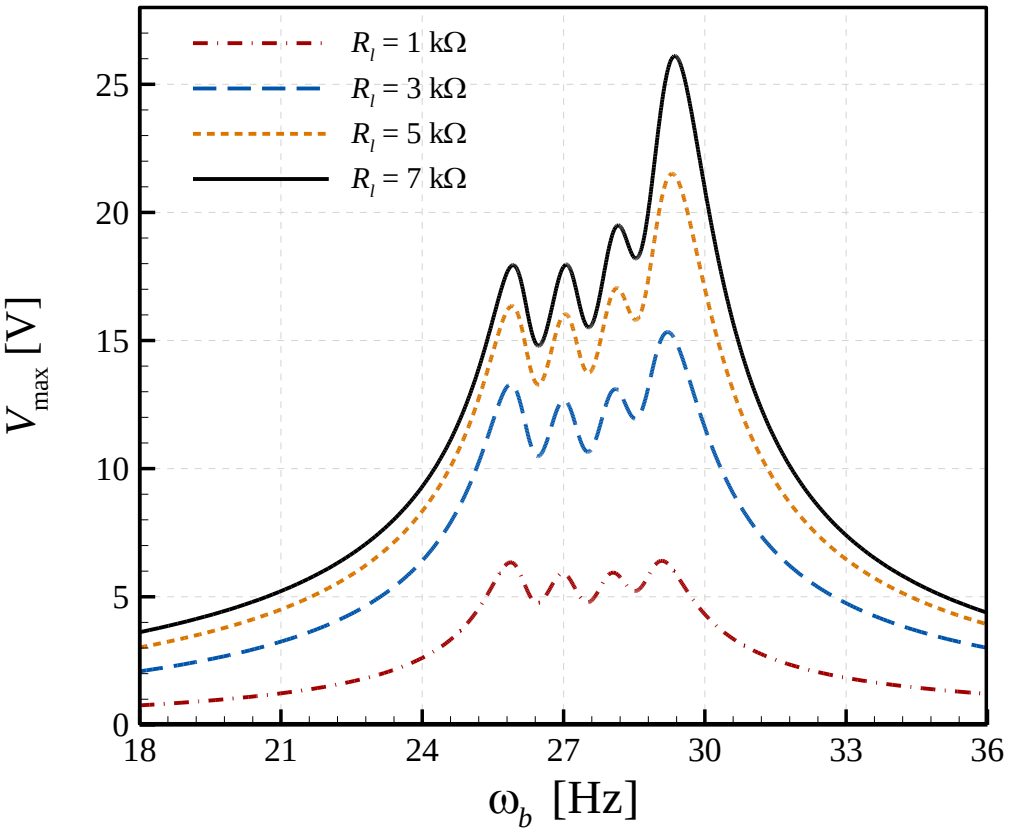

Fig.6. Effect of load resistance on frequency responses of an array of 4 PBs in parallel; maximum (a) power output and (b) voltage output.

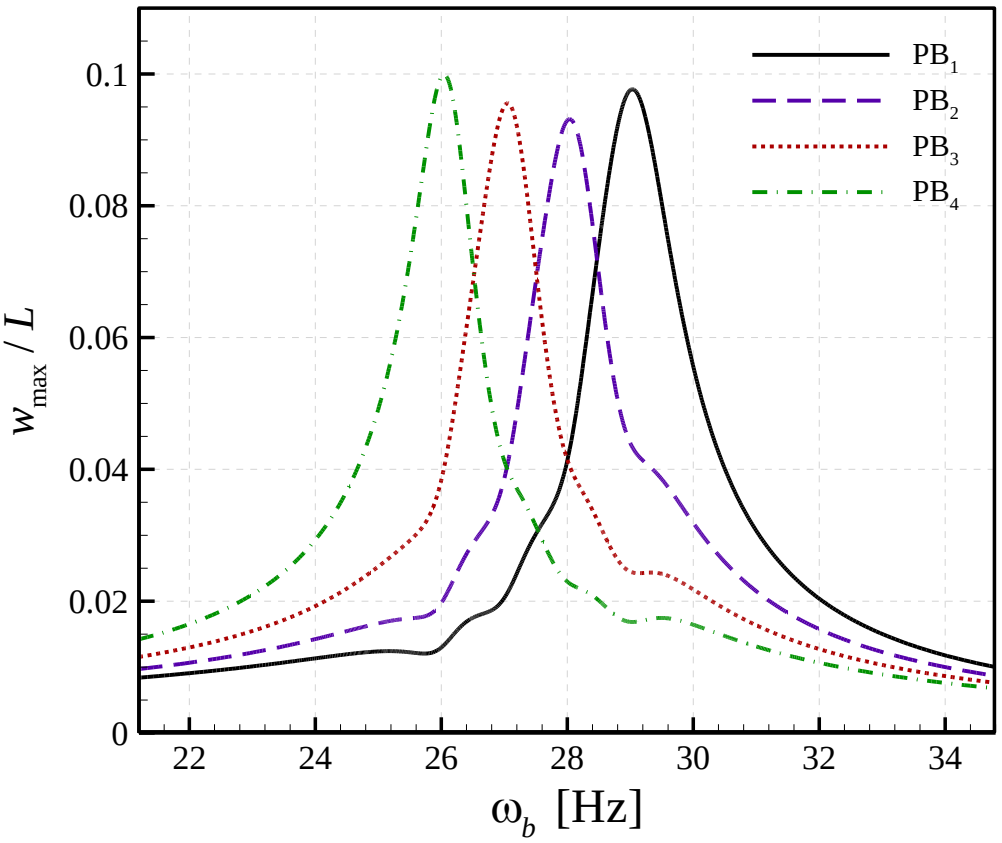

Fig.7. Frequency responses of the maximum tip displacement of an array of 4 PBs connected in parallel when R_l = 4.0 kΩ.

(a)

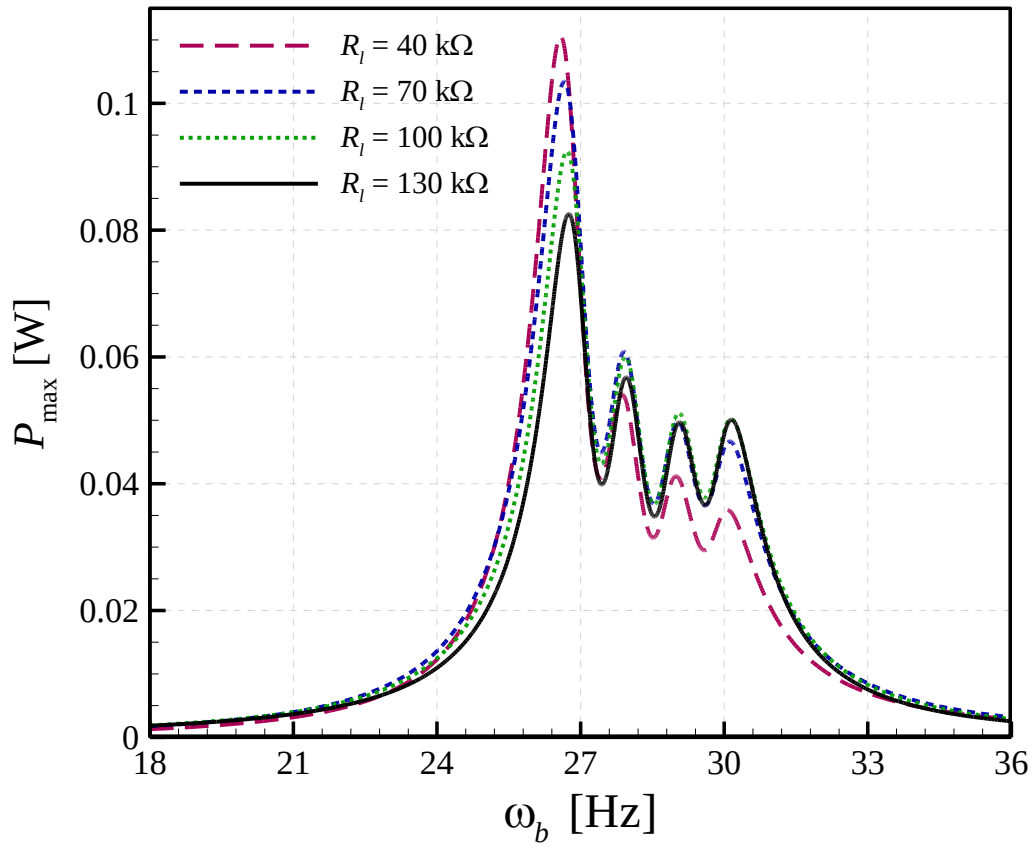

(b)

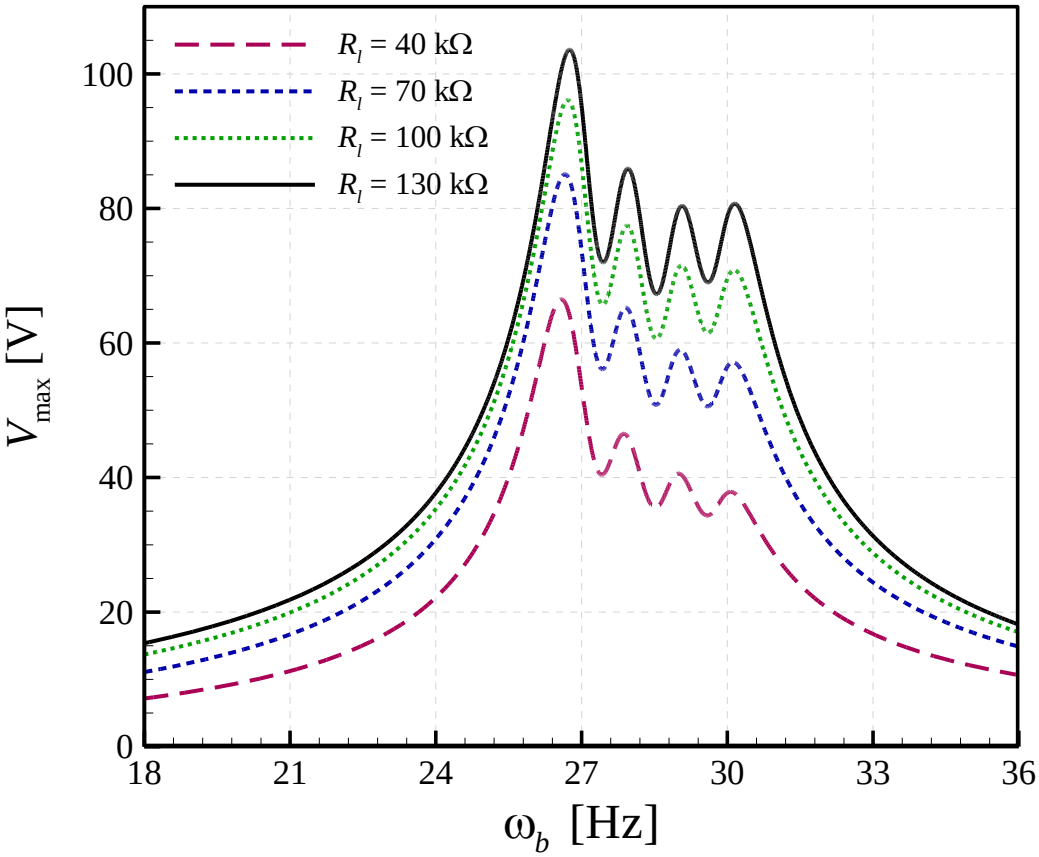

Fig.8. Effect of load resistance on frequency responses of an array of 4 PBs in series; maximum (a) power output and (b) voltage output.

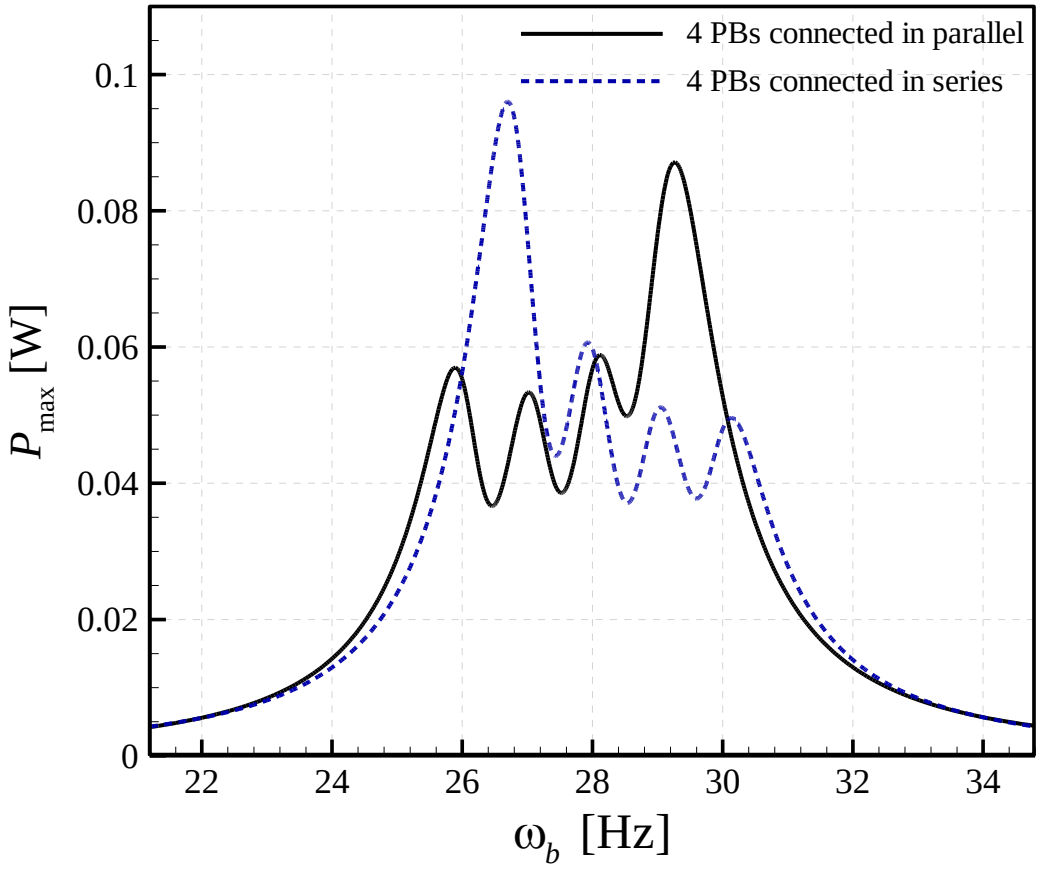

Fig.9. Frequency response of the maximum power output of an array of 4 PBs connected in parallel versus that in series. R_l = 4.0 kΩ for parallel connection and 90.0 kΩ for series connection.

(a)

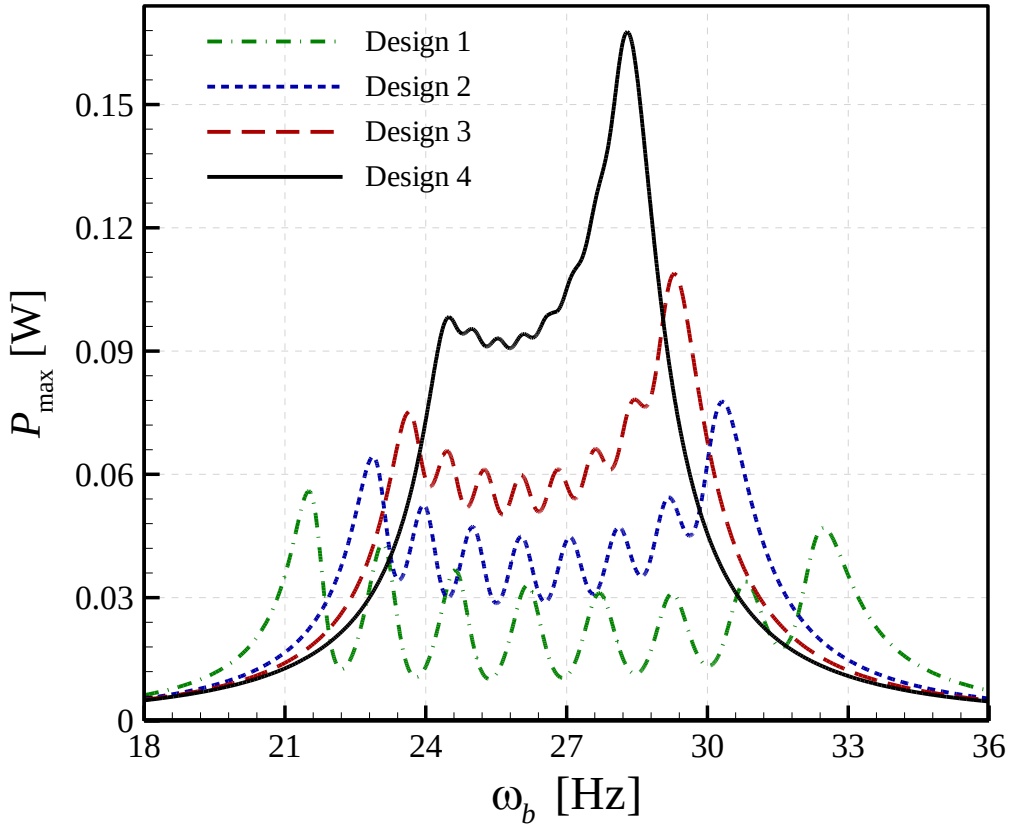

(b)

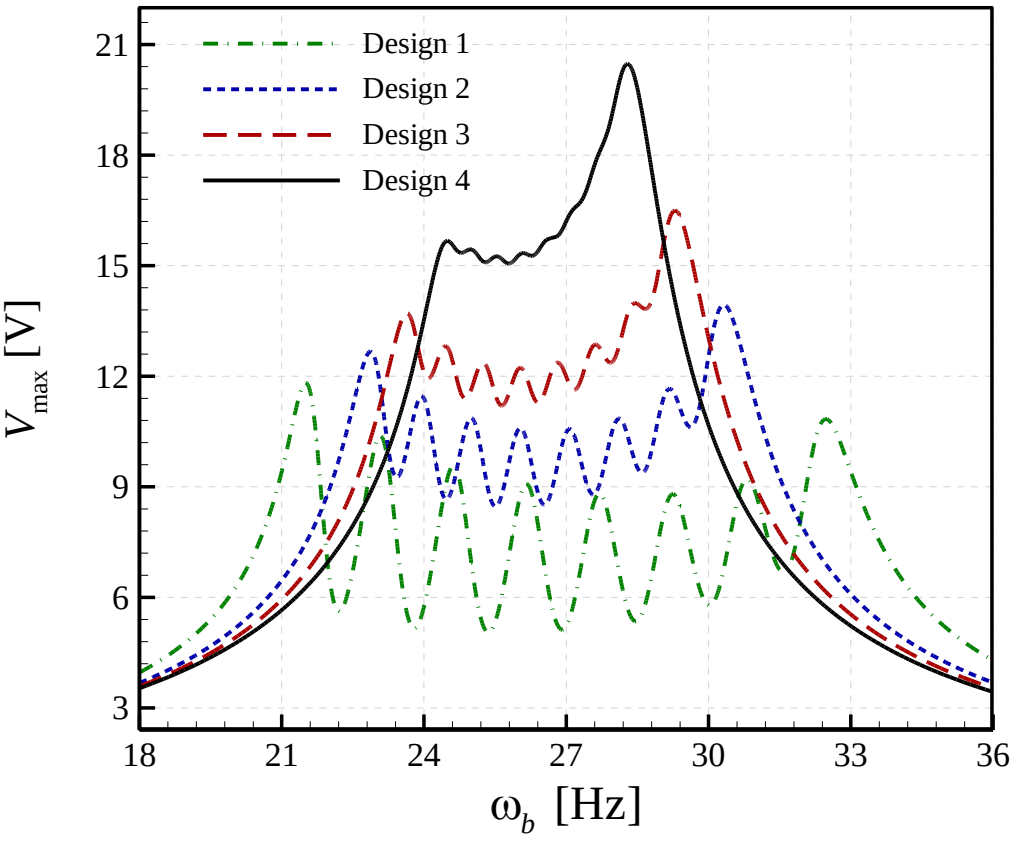

Fig.10. Frequency responses of the maximum (a) power output and (b) voltage output of different designs of an array of 8 PBs connected in parallel. The difference between the PBs' short-circuit natural frequencies is 1.5 Hz for design 1, 1.0 Hz for design 2, 0.75 Hz for design 3, and 0.5 Hz for design 4.

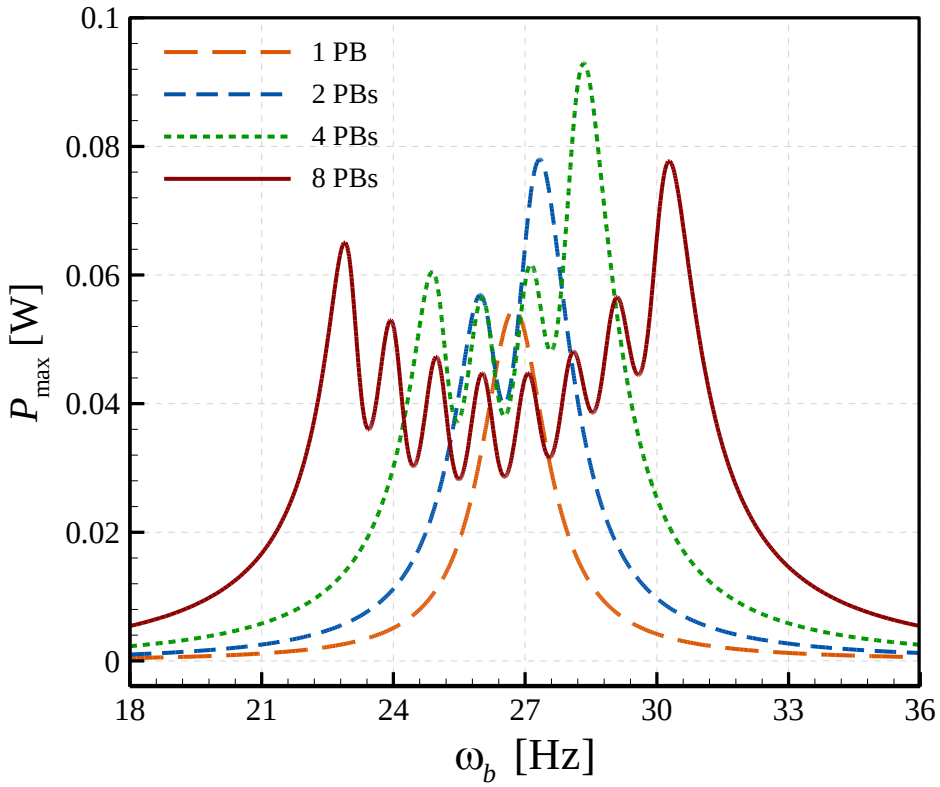

Fig.11. Frequency responses of various arrays of PBs connected in parallel for maximum power output. The PBs' short-circuit natural frequencies are 1 Hz apart for the cases with more than 1 PB.

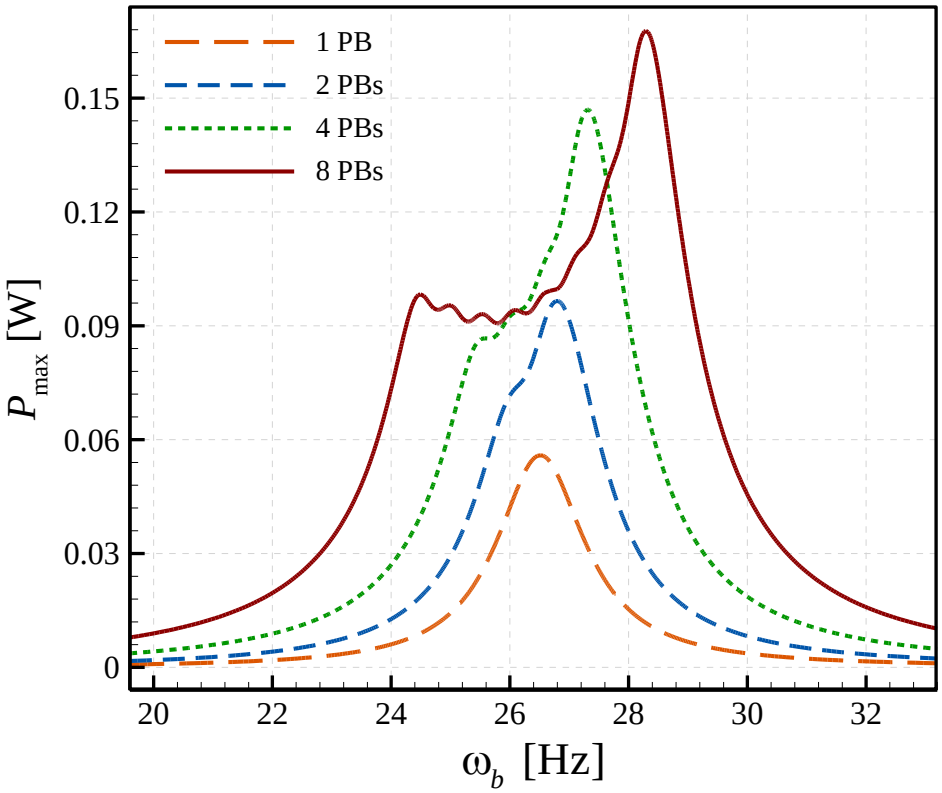

Fig.12. Frequency responses of various arrays of PBs connected in parallel for maximum power output. The PBs' short-circuit natural frequencies are 0.5 Hz apart for the cases with more than 1 PB.

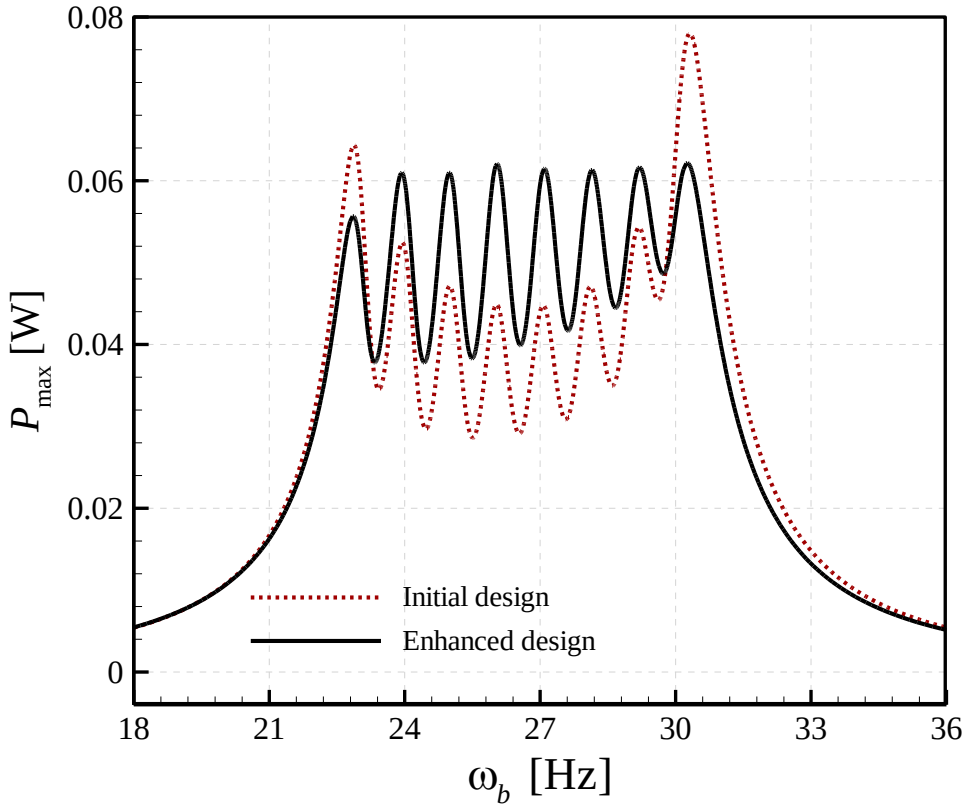

Fig.13. Frequency responses of two array designs for 8 PBs connected in parallel for maximum power output. The PBs' short-circuit natural frequencies are 1 Hz apart.

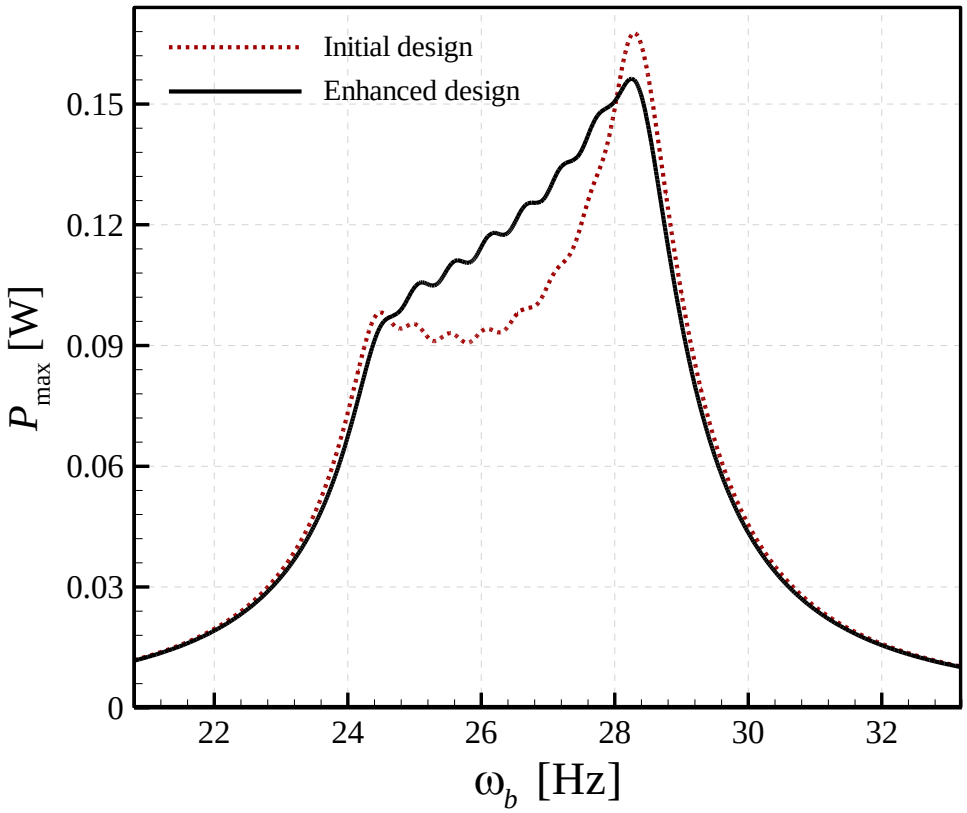

Fig.14. Frequency responses of two array designs for 8 PBs connected in parallel for maximum power output. The PBs' short-circuit natural frequencies are 0.5 Hz apart.

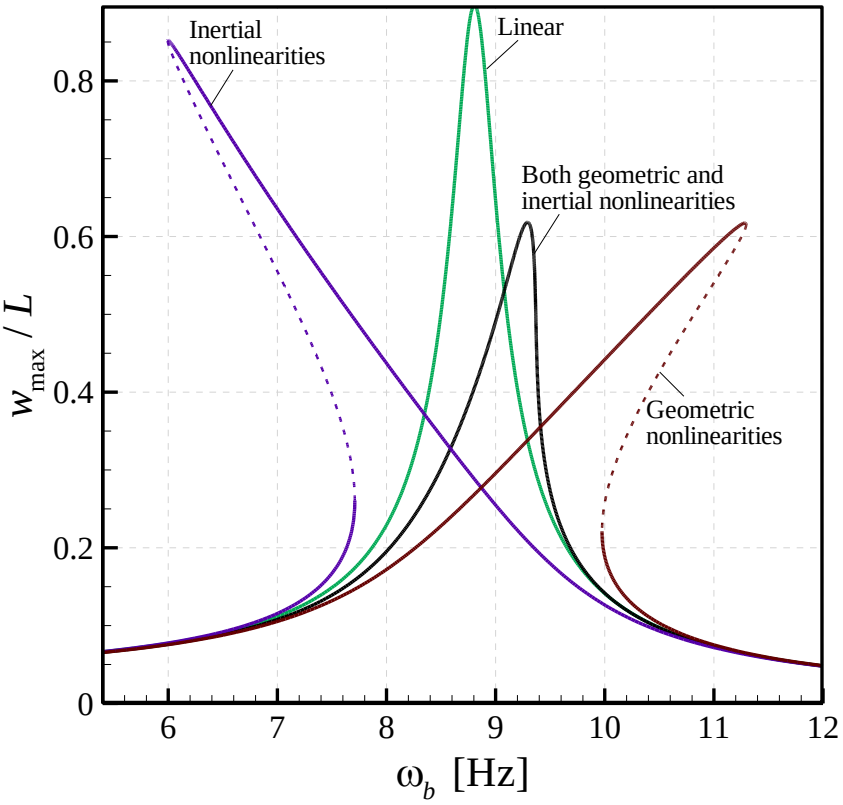

Fig.15. Effect of various sources of nonlinearity on frequency responses of a piezoelectric harvester; maximum tip transverse displacement.

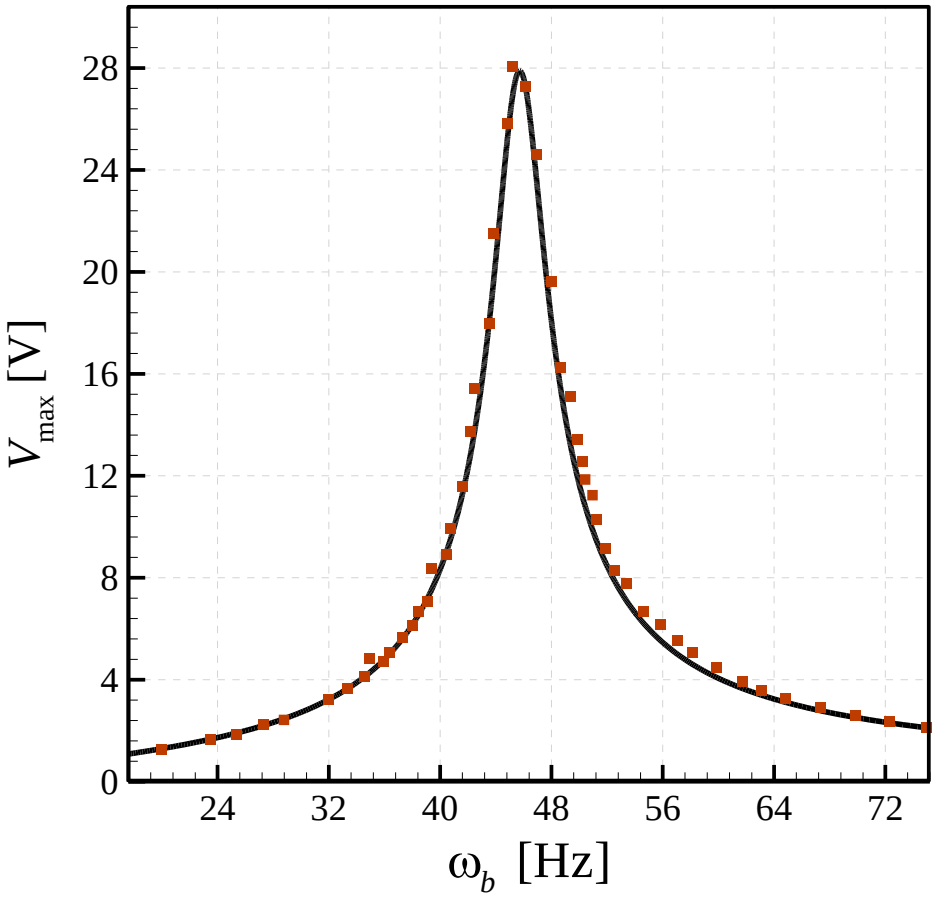

Fig.16. Frequency behaviour of a single piezoelectric bimorph in series; solid line shows the results obtained using the proposed model and symbols indicate those observed experimentally in Ref. [21].